Master's Thesis

Indoor Localization Using Ultra-Wideband Radio Signal

Yitong Quan

2

Declaration

I hereby declare, that I am the sole author and composer of my thesis and that no other sources or learning aids, other than those listed, have been used. Furthermore, I declare that I have acknowledged the work of others by providing detailed references of said work.

I hereby also declare, that my Thesis has not been prepared for another examination or assignment, either wholly or excerpts thereof.

_____	_____
Place, Date	Signature

Abstract

Recently, indoor localization has obtained more and more interest within the research community, due to the wide range of services it can provide. Among the vast indoor ranging technologies, Ultra-wideband (UWB) is one of the most popular ones, due to its many advantages, such as superior penetration properties, robust performance in the presence of non-line-of-sight (NLOS) propagation, large channel capacity and very low operating power. This master thesis presents a novel UWB ranging system with sampling rate of 1.5 Hz and data missing rate of 0.16. Besides, four localization algorithms based on extended Kalman filter (EKF) and optimization method (OM), have been built and tested with measurement data collected by this ranging system. These algorithms have been proved that they can recover the trajectories of the moving target, with the root-mean-square error (RMSE) varies from 0.20 m to $0.25\,m$ in position estimation and 0.13 m/s to 0.37 m/s in velocity estimation.

Keywords: indoor localization, ultra-wideband, extended Kalman filter, optimization method for localization, NLOS mitigation.

Zusammenfassung

In letzter Zeit hat die Lokalisierung in Innenräumen aufgrund der großen Bandbreite an Dienstleistungen, die sie bieten kann, in der Forschungsgemeinschaft mehr und mehr Beachtung gefunden. Unter den zahlreichen Ranging Technologien in Innenräumen ist die Ultra-Breitband-Technologie (UWB) aufgrund ihrer vielen Vorteile, wie überlegene Penetrationseigenschaften, hohe Robustheit bei Nicht-Sichtverbindung, große Kanalkapazität und sehr geringe Betriebsleistung, eine der beliebtesten. Diese Masterarbeit präsentiert ein neuartiges UWB-Entfernungsmesssystem mit einer Abtastrate von 1,5 Hz und einer Datenverlustrate von 0,16. Außerdem wurden vier Lokalisierungsalgorithmen basierend auf dem erweiterten Kalman-Filter (EKF) und der Optimierungsmethode (OM) entworfen und mit Messdaten aus dem UWB-Entfernungsmesssystem getestet. Diese Algorithmen haben bewiesen, dass sie die Trajektorie des sich bewegenden Ziels wiederherstellen können, wobei die Wurzel des mittleren quadratischen Fehlers (RMSE) bei der Positionsschätzung von $0,20\,\mathrm{m}$ bis $0,25\,\mathrm{m}$ und bei der Geschwindigkeitsschätzung von $0,13\,\mathrm{m/s}$ bis $0,37\,\mathrm{m/s}$ variiert.

Stichwörter: Lokalisierung in Innenräumen, Ultra-Breitband-Technologie, erweitertes Kalman-Filter, Optimierungsmethode für Lokalisierung, NLOS Mitigation.

Contents

Nomenclature

Abbrevations

Abbrevation	Meaning
DSTWR	double sided two way ranging
EKF	extended Kalman filter
EKF-LWCR	extended Kalman filter Linear with Weighted Combination based on Residua
EKF-MC1	EKF using Measurements Combination 1
EKF-MC2	EKF using Measurements Combination 2
FBW	fractional bandwidth
FCC	Federal Communications Commission
GPS	Global Positioning System
KF	Kalman filter
LOS	line-of-sight
MC	measurement combination
NLOS	non-line-of-sight
OM	optimization method
PSD	power spectral density
RMSE	root-meas-square error
RTC	real time counter
RTD	round-trip delay time
RTT	round-trip time
SDSTWR	symmetrical double sided two way ranging
SNR	signal-to-noise ratio
SSTWR	single sided two way ranging
ToA	time of Arrival
ToF	time of flight
TWR	two way ranging
UWB	ultra-wideband
WLAN	wireless local area network

List of Figures

List of Tables

1 Introduction

Nowadays the continuous rise of interest towards indoor localization can be observed. Real-time accurate indoor position information is required by many innovative applications, such as tracking goods in warehouses, guiding people in exhibitions, shopping malls, hospitals and airports, detecting the location of firemen inside a building on fire. In the past decades, many technologies have been applied for localization purpose. The Global Positioning System (GPS) is one of the widely used technologies for outdoor localization. Satellites broadcast signals containing their positions and timing. The receivers on the surface of the Earth obtain these signals and calculate their distances to satellites, then estimate their own positions base on trilateration [1]. GPS-enabled smartphones typically have an accuracy within 4.9 m [2]. A study shows that ever higher accuracy up to 1.9 m can be achieved by particular GPS system [3]. However, signal attenuation caused by walls and roofs makes the power of GPS signal significant low inside buildings [4]. For this reason, GPS is not suitable for the indoor application. Localization based on ultrasound technology can achieve accuracy with centimeter-level for indoor environment [5]. The ultrasound-based localization system *ASSIST* built by company *Telocate* can locate a target with error margin of 0.3 m [6]. Some ultrasound based systems [7], [8] can even achieve 0.1 m accuracy. These ultrasound based systems calculate the distance between the transmitter and the receiver based on Time of Flight (ToF) technique and the speed of sound. However, in comparison to radio frequency signal, the ultrasound signal has the drawback that its velocity varies significantly as temperature and humidity change [9]. Besides, the accuracy of ultrasound-based localization system is easily effected by Non-Line-of-Sight(NLOS) propagation caused by signals reflection from the obstacles. Indoor localization base on Ultra-wide Band (UWB) radio signal uses ToF and speed of light to calculate distances. Unlike ultrasound signal, the UWB signal can effectively penetrate through a variety of materials inside building, such as walls, doors and furniture. That is because the broad range of the UWB frequency spectrum includes also low frequencies. And these low frequencies signal have long wavelengths, allowing them to penetrate a variety of materials. Besides, UWB system uses carrierless, very short-duration-pulses (nanosecond) for information transmission and reception. The duration of pulses is so short that the reflected pulses have a very short time-window of opportunity to collide with the Line-of-Sight (LOS) signals, thus less likely to cause degradation [10], [11]. This property makes UWB system less sensitive to multipath propagation. These two advantages make UWB a very good candidate for indoor localization. Figure 1.1 shows the PCB of one communication node of an UWB measurement system, which is developed by Patrick Fehrenbach [12]. This PCB contains a transceiver on board,

and it can be served as both anchor node and mobile tag. It has been shown that this system can measure distances up to 10 m with the accuracy of 25 cm indoor [12]. However, the sampling rate of this system is only 0.2 Hz and the measurement obtained rate is only 0.46. The values of these two rates are so low, that it is difficult to achieve localization with high resolution.
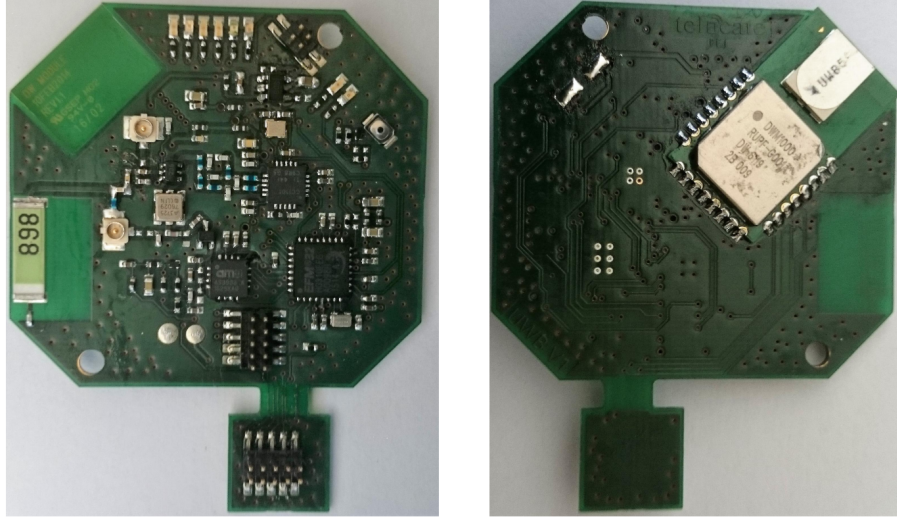
Figure 1.1: Node of UWB measurement system by Patrick Fehrenbach [12]

.

Noisy measurement data cannot be avoided due to the stochastic noises and errors. Besides, other problems, such as measurement data missing and unable to require the positions of anchor nodes, also make it difficult to localize a moving target (here the mobile tag) without extra help, such as estimation methods. There are numerous estimation methods in use, but the two main methods are sequential Bayesian estimation and optimization approach [13]. The sequential Bayesian estimation estimates the states, for example, the positions of the mobile tag, based on measured data, also the prior information, such as the positions of the anchor nodes. On the other hand, the optimization approach estimates the states based only on measurements without prior information.

Even with the above mentioned advantages of UWB, the NLOS errors can still not be avoided. To reduce the impact of NLOS errors on the accuracy of the localization. [14] proposes a residual test (RT) that can identify NLOS errors based on the distribution of the residuals, which are the square differences between the estimates and the true position. [15] proposes a residual weighting algorithm (RWGH) to mitigate the NLOS errors in localization without identifying them.

The aim of this master thesis is to realize accurate localization using the UWB ranging system built by Patrick Fehrenbach [12]. To achieve this aim, two main tasks are done. The first task is performance improvements of the UWB ranging system, which includes the increases in sampling rate and measurement obtained rate. The second task is the implementations of algorithms for accurate localization.

These algorithms include extended Kalman filter (EKF) from catalog sequential Bayesian estimation and Optimization Method (OM) for localization from catalog optimization approach. Also, a NLOS errors mitigation algorithms, Linear Weighted Combination based on Residual (LWCR), is proposed and tested.

This master thesis is presented in the following structure. Chapter 2 explains the theoretical background knowledge, which includes UWB, Two Way Ranging(TWR), trilateration, EKF and OM. Chapter 3 shows the improvements of the UWB ranging system, and evaluates the performance of the improved system from the perspectives of sampling rate and data obtain rate. Chapter 4 demonstrates the calibrations for the ranging system and analyzes the distributions of the measurement data. Chapter 5 explains the localization algorithms used in this thesis, including EKF, OM and LWCR. Chapter 6 demonstrates the results of simulations and real-world experiments. These results include the performance of the implemented EKF, OM, and LWCR, from the perspective of the accuracy of the localization. Chapter 7 summarizes the achievement of this thesis.

2 Theoretical Background

In this chapter, the theoretical foundations related to this thesis will be explained, which are trilateration, UWB based distance measurement and EKF.

2.1 Trilateration

For position determination in this thesis, trilateration is used, which is described as followed:

In a two dimensional space, for instance, to determine the position of a point, at least distances to 3 different fixed points are required, except for the case that these 3 fixed positions lie on the same line.

When the exact distances from a mobile tag to 3 anchor nodes are known, the position of this mobile tag is the intersection point of circles around the nodes with the corresponding radius. As shown in Figure 2.1
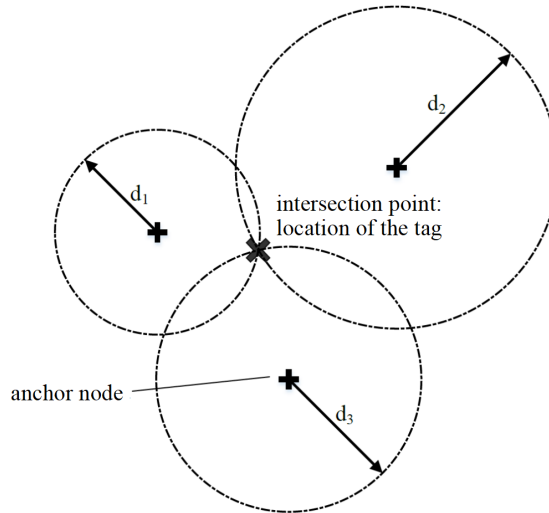
Figure 2.1: Localization of a mobile tag with trilateration.

Due to the inherent error of hardware, reflection or multipath propagation [16], noises are added to the distance measurements from a mobile tag to anchor nodes, resulting in that the circles do not intersect at a unique point.

2.2 Ultra-wideband

2.2.1 Definition and Properties

Ultra-wideband (UWB) is a revolutionary radio technology for communications, with the properties of low energy consumption level for short-range, high-bandwidth, covering large portion of the radio spectrum [17]. In February 2002, the Federal Communications Commission (FCC) has authorized the unlicensed use of UWB in frequency range of $3.1 \sim 10.6\ GHz$. UWB signal is defined as those that has a large absolute 10 dB bandwidth of more than 500 MHz, or has a fractional bandwidth (FBW) that larger than 20%. The FBW is defined by Equation 2.1, where f_H and f_L are the upper and lower cutoff frequencies at -10 dB point of a UWB spectrum.

$$FBW = \frac{2(f_H - f_L)}{f_H + f_L} \tag{2.1}$$

To avoid interference with other already existing communication technologies that operating in the same UWB allocated bands, such as Wireless Local Area Network (WLAN) IEEE 802.11a. The FCC requires that the power emission level of the UWB signal must be sufficiently low. Specifically, the maximum allowed power spectral density (PSD) should be lower than -41.25 dBm/MHz. PSD is defined as the ratio between power transmitted in watts and bandwidth of the transmitted signal in hertz. Due to its huge bandwidth, the PSD of a UWB signal can be very low comparing to other communication technologies. This low PSD makes the UWB signals like a background noise to most of the existing wireless communication devices. For this reason, the UWB system can coexist well with other radio communication systems. Figure 2.2 shows the PSD of UWB together with other technologies.
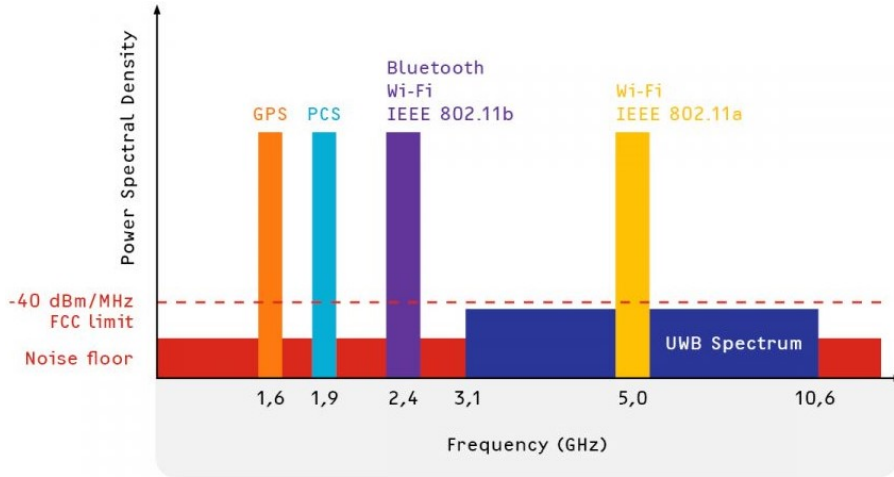
Figure 2.2: PSD of UWB versus other radio communication systems [18].

Another importance feature of an UWB system is that it uses carrierless, short-duration pulse with a low duty cycle for information transmission. The pulse dura-

tion is normally in the rang of picosecond (10^{-12} s) to nanosecond (10^{-9} s), and the duty cycle is normally less than 0.5% [10]. A duty cycle is defined as the ration of the present time of a pulse to the total transmission time. A low duty cycle results a low average transmission power in UWB system, i.e., a longer battery life can be obtained, which is very crucial to devices equipped powered by battery. [10] [11] [19].

2.2.2 Advantages of UWB

The nature of covering wide bandwidth and using short-duration pulses offers UWB the following advantage over narrowband:

Large channel capacity. Channel capacity is defined as the maximum amount of information that can be transmitted over a communication channel per second when noises are present. According to Shannon-Hartley theorem, the channel capacity C can be calculated as Equation 2.2,

$$C = B \log_2 \left(1 + \frac{S}{N} \right), \tag{2.2}$$

where B is the bandwidth of the channel, S is the average received signal power over the bandwidth and N s the average power of the noise and interference over the bandwidth. As shown in Equation 2.2, the capacity of the channel is linearly increases with the bandwidth. Therefore UWB system has large channel capacity by its nature of occupying large bandwidth.

Ability to work with low signal-to-noise ratio (SNR). As shown in Equation 2.2, the channel capacity is only logarithmically grow with SNR. Due to its wide bandwidth, UWB system can still able to work in severe conditions where the SNR is low.

Low interference with other existing signal. As described in , the low PSD of the UWB signals make them unlikely to interference with other existing signal.

Superior penetration property. The wide range of the UWB spectrum includes also low frequencies, which have long wavelengths. With these long wavelengths, the UWB signals can penetrate a multiplicity of materials, including doors and walls.

High performance against multipath propagation. By using the very short-duration pulses, UWB systems are less sensitive the multipath propagation, compare to the systems using narrowband signals. Since the duration of UWB pulses is in the range of nanoseconds, the reflected pulses have extremely short windows of opportunity to collide with the light-of-sight pulses.

Simple transceiver architecture. Since the UWB transmission is carrierless, components, such as the mixers and and local oscillators for frequency conversion, are no longer required.

Low power. The simple transceiver architecture and the very low duty for transmission make UWB system consumes less power. This makes the UWB very suitable for battery-powered devices.

Among these mentioned advantages, the superior penetration property and high performance against multipath propagation make the UWB an ascending option for ranging for indoor environment, due to the presence of obstacles, such as walls, doors and furniture. [10] [11] [19].

2.3 Distance Measurements

One way to measure the distance d between the mobile tag and an anchor node, is to count the signal travel time Δt between the sending time the receipt time, based on the relation:

$$d = \Delta t \cdot c ,\qquad(2.3)$$

where c is the speed of the UWB signal, which is the speed of light, equals to 299,792,458 m/s, or approximately 3×10^8 m/s.

In order to measure the above mentioned signal travel time, the ToF technique, or sometimes called Time of Arrival (ToA), is used. ToF requires a precise time synchronization between each pair of mobile tag and anchor nodes, since the signal travel time is calculated base on the local timestamps of these devices.

To avoid the time synchronization, Round-Trip Time (RTT), also called Round-Trip Delay time (RTD) can be used. The principle of RTT is shown in Figure 2.3. In this procedure, two messages are sent sequentially. The first message is sent from the anchor node to the mobile tag. Then the mobile tag reply to the anchor node after some delay, due to internal processing in mobile tag, or due to the purpose of making specified transmission time predictable and aligned with the transmit timestamp [20]. In Figure 2.3, t_0, t_3, t_2, t_1 are the timestamps of sending and receiving messages in anchor node mobile tag. After message 1 is received, mobile tag will send t_2, t_1 to anchor node through message 2. The distance can be calculated using these timestamps as Equation 2.4.

When t_2 is equal to t_1, then the above RTT is the procedure of ranging in Radar(radio detection and ranging).

$$d = \frac{(t_0 - t_3) - (t_2 - t_1)}{2} \cdot c\qquad(2.4)$$

Following are 3 of the main implementations of RTT.

- Single Sided Two Way Ranging (SSTWR).

SSTWR is the basic implementation of RTT. The mobile tag send a message to the anchor node, which responds with another message back to mobile tag to accomplish the measuring process, as illustrated in Figure 2.4. And each devices record their transmission and reception timestamps of the messages, T_{round} is defined as the subtraction of reception timestamp and transmission timestamp in mobile tag, while T_{reply} as the subtraction of transmission timestamp and transmission
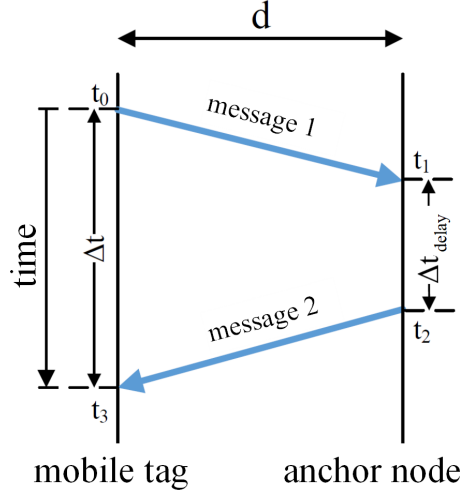
Figure 2.3: Principle of RTT [21].

timestamp in anchor node. So the time of flight between these two devices, T_{ToF} can be calculated by Equation 2.5.
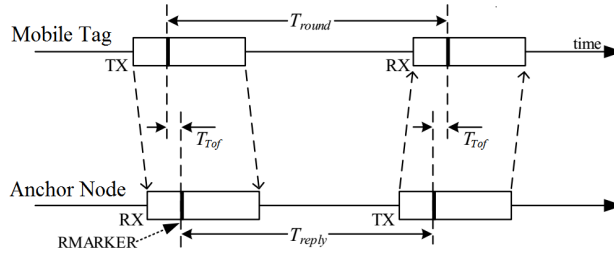
Figure 2.4: Illustration of SSTWR [20].

$$T_{ToF} = \frac{T_{round} - T_{reply}}{2} \tag{2.5}$$

Then the distance between mobile tag and anchor node can be calculated by Equation 2.6.

$$d = T_{ToF} \cdot c \tag{2.6}$$

SSTWR has the advantage of time and energy saving, since only 2 messages are sent for one measuring. However it has the disadvantage of inaccuracy when T_{reply} is big, since the T_{round} and T_{reply} are measured in two different devices with different local clock offset [20].

- Double Sided Two Way Ranging (DSTWR).

DSTWR is an extended version of SSTWR, combining two RTT time measurements, and has a smaller error about the ToF result in comparison with SSTWR even for large T_{reply} [20].

Figure 2.5 illustrates the operation of DSTWR. The mobile tag first sends a message to the anchor node. Then the anchor node responds back to the mobile tag with another message, which serves as the end of the first RTT measurement and the beginning of the second RTT measurement. Finally, the mobile tag sends back a third message to the anchor node and ends this ranging.
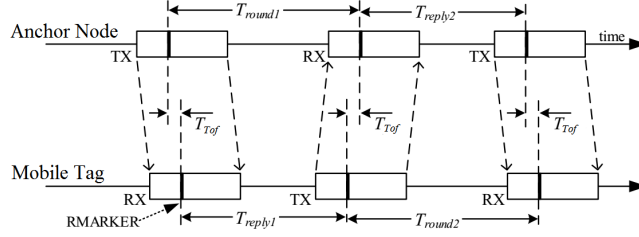
Figure 2.5: Illustration of DSTWR [20].

The T_{ToF} can be calculated by Equation 2.7 [20].

$$T_{ToF} = \frac{T_{round1} \times T_{round2} - T_{reply1} \times T_{reply1}}{T_{round1} + T_{round2} + T_{reply1} + T_{reply1}} \qquad (2.7)$$

DSTWR has the advantage of small error in calculating ToF compare to SSTWR, and the disadvantage of requiring multiplication and division operations [20].

- Symmetrical Double Sided Two Way Ranging (SDSTWR).

SDSTWR is a special case of DSTWR where T_{reply1} and T_{reply2} are required to be equal. Then the T_{ToF} can be calculated by Equation 2.8 [20].

$$T_{ToF} = \frac{T_{round1} - T_{reply2} + T_{round2} - T_{reply1}}{4} \qquad (2.8)$$

SDSTWR has the advantage of low power consumption for micro-controller, since it requires only addition, subtraction and division by 4. However it has the disadvantage of long measuring time, since the T_{reply1} and T_{reply2} have to be the same, which means the greater value among these two has to be chosen.

2.4 Kalman Filter

The positions of a moving mobile tag can be localized using the measured distances to anchor nodes as illustrated in section 2.1. But in some situations, for example, some of the measurements are missing, or the measurements from different devices

have different noise level, or the measurements are too noisy, the basic implementation of section 2.1 would has difficulty to solve the localization problem. To tackle this difficulty, the Kalman filter can be used.

Kalman filter (KF) is one of the well-known algorithms for stochastic estimation using noisy measurements. It is named after Rudolf E. Kalman. Since it was introduced, KF has been numerously applied in many area, such as autonomous navigation of vehicles and robotic motion planning.

For simplicity, the following introduction about KF is about its discrete form, since this is the form used in this thesis.

The KF substantially uses a series of observations over time to make better estimations about system states, compare to those based purely on one measurement. In a KF model, the current state $\mathbf{x}_k$ is developed from last state $\mathbf{x}_{k-1}$ with the state transition matrix $\mathbf{A}$, control-input vector $\mathbf{u}_k$, control-state-transition matrix $\mathbf{B}$ and process noise $\mathbf{w}_k$, as shown in Equation 2.9,

$$\mathbf{x}_k = \mathbf{A}\mathbf{x}_{k-1} + \mathbf{B}\mathbf{u}_k + \mathbf{w}_k \tag{2.9}$$

and the observation $\mathbf{z}_k$ of the current state $\mathbf{x}_k$ can be obtained with the help of the observation-state-transition matrix $\mathbf{H}_k$ and observation noise $\mathbf{v}_k$, as shown in Equation 2.10,

$$\mathbf{z}_k = \mathbf{H}_k\mathbf{x}_k + \mathbf{v}_k \tag{2.10}$$

The $\mathbf{w}_k$ and $\mathbf{v}_k$ in Equation 2.9 and Equation 2.10 are assumed to be Gaussian white noise with covariances $\mathbf{Q}_k$ and $\mathbf{R}_k$, i.e. $\mathbf{w}_k \sim \mathcal{N}(0, \mathbf{Q}_k)$ and $\mathbf{v}_k \sim \mathcal{N}(0, \mathbf{R}_k)$, which are independent distributed.

The KF is an implementation a recursive estimator with the type of predictor-corrector [22]. It contains two steps in each recursive, i.e. prediction and correction. The prediction step projects the current estimates of state and error covariance over time to gain a priori estimation for the next time step. And the correction step uses the new obtained measurement as 'feedback' to correct the a priori estimation from last prediction step, and obtains a new improved estimation, known as a posteriori estimation.

The mathematical equations for prediction step is illustrated in Equation 2.11 and Equation 2.12,

$$\hat{\mathbf{x}}_k^- = \mathbf{A}\hat{\mathbf{x}}_{k-1} + \mathbf{B}\mathbf{u}_k \tag{2.11}$$

$$\mathbf{P}_k^- = \mathbf{A}\mathbf{P}_{k-1}\mathbf{A}^{\mathrm{T}} + \mathbf{Q}_k \tag{2.12}$$

where $\hat{\mathbf{x}}_k^-$ and $\mathbf{P}_k^-$ are the a priori estimation of state vector and error covariance at time step k, $\hat{\mathbf{x}}_{k-1}$ and $\mathbf{P}_{k-1}$ are the a posteriori estimation from last time step $k-1$, $\mathbf{A}$, $\mathbf{B}$, $\mathbf{u}_k$ and $\mathbf{Q}_k$ are the state-transition matrix, the control-input matrix, control-input vector and the covariance of the process noise at time step k.

The mathematical equations for correction step is illustrated in Equation 2.13, Equation 2.14, Equation 2.15 and Equation 2.16,

$$\mathbf{K}_k = \mathbf{P}_k^- \mathbf{H}^\mathrm{T} (\mathbf{H}\mathbf{P}_k^- \mathbf{H}^\mathrm{T} + \mathbf{R})^{-1} \tag{2.13}$$

$$\mathbf{r}_k = \mathbf{z}_k - \mathbf{H}\hat{\mathbf{x}}_k^- \tag{2.14}$$

$$\hat{\mathbf{x}}_k = \hat{\mathbf{x}}_k^- + \mathbf{K}_k \mathbf{r}_k \tag{2.15}$$

$$\mathbf{P}_k = (\mathbf{I} - \mathbf{K}_k \mathbf{H})\mathbf{P}_k^- \tag{2.16}$$

where $\hat{\mathbf{x}}_k$ and $\mathbf{P}_k$ are the a posteriori estimations of the state vector and error covariance at time step k, which will be severed as a priori estimations for the next recursive at time step $k+1$. $\mathbf{K}_k$ is the optimal Kalman gain. $\mathbf{r}_k$ is the measurement pre-fit residual. $\mathbf{H}$ is the observation matrix which maps the current state vector into the observed vector. $\mathbf{z}_k$ is the observation, i.e, the measurement vector. $\mathbf{R}$ is the covariance of the observation noise. $\mathbf{I}$ is a identity matrix.

Note that the state-transition matrix $\mathbf{A}$, the control-input matrix $\mathbf{B}$ and the observation matrix $\mathbf{H}$ are applied into the equations with the matrix multiply operator, which means that they can only perform well when the transitions between states, inputs and observations are linear. However for the non-linear cases, which is required for this thesis, other variant of KF can be used, such as extended Kalman filter. [22] [23]

2.5 Extended Kalman Filter

The Extended Kalman Filter (EKF) is an extension of KF, which can be used to deal with the cases where the state transition and observation-state-transition is not linear, by linearization via Taylor expansion at the current estimate of the mean and covariance.

In comparison to Equation 2.9 and Equation 2.10, the relations between current state, its previous state and its observation are as shown in Equation 2.17 and Equation 2.18,

$$\mathbf{x}_k = f(\mathbf{x}_{k-1}, \mathbf{u}_k) + \mathbf{w}_k \tag{2.17}$$

$$\mathbf{z}_k = h(\mathbf{x}_k) + \mathbf{v}_k \tag{2.18}$$

where $f(\cdot)$ is the function for state transition model, and $h(\cdot)$ is the function for observation model. Both $f(\cdot)$ and $h(\cdot)$ can be non-linear functions.

The equations for prediction step of EKF are listed in Equation 2.19 and Equation 2.20,

$$\hat{\mathbf{x}}_k^- = f(\hat{\mathbf{x}}_{k-1}, \mathbf{u}_k) \tag{2.19}$$

$$\mathbf{P}_k^- = \mathbf{A}_{k-1}\mathbf{P}_{k-1}\mathbf{A}_{k-1}^{\mathrm{T}} + \mathbf{Q}_k \tag{2.20}$$

where $\mathbf{A}_{k-1}$ is the Jacobian matrix of $f(\cdot)$ with respect to $\hat{\mathbf{x}}_{k-1}$, as shown in Equation 2.21

$$\mathbf{A}_{k-1} = \left.\frac{\partial f}{\partial \mathbf{x}}\right|_{\hat{\mathbf{x}}_{k-1}} \tag{2.21}$$

The mathematical equations for correction step is illustrated in Equation 2.22, Equation 2.23, Equation 2.24 and Equation 2.25,

$$\mathbf{K}_k = \mathbf{P}_k^-\mathbf{H}^{\mathrm{T}}(\mathbf{H}\mathbf{P}_k^-\mathbf{H}^{\mathrm{T}} + \mathbf{R})^{-1} \tag{2.22}$$

$$\mathbf{r} = \mathbf{z}_k - \mathbf{H}\hat{\mathbf{x}}_k^- \tag{2.23}$$

$$\hat{\mathbf{x}}_k = \hat{\mathbf{x}}_k^- + \mathbf{K}_k\mathbf{z}_k \tag{2.24}$$

$$\mathbf{P}_k = (\mathbf{I} - \mathbf{K}_k\mathbf{H})\mathbf{P}_k^- \tag{2.25}$$

where $\mathbf{H}$ is the Jacobian matrix of $h(\cdot)$ with respect to $\hat{\mathbf{x}}_k^-$, as shown in Equation 2.26

$$\mathbf{H} = \left.\frac{\partial h}{\partial \mathbf{x}}\right|_{\hat{\mathbf{x}}_k^-} \tag{2.26}$$

3 Hardware Improvement

In this chapter, the working principle of the UWB distances measurement system is introduced. Then the shortages of this system are illustrated. Finally, the improvements done to this system are be explained.

3.1 Communication Procedure

The system contains one base station, one mobile tag and several anchor nodes. The mobile tag is the target to be localized. The anchor nodes are mounted in the infrastructure, with fixed positions. In order to save energy, the initial states of the mobile tag and the anchor nodes are sleep mode. When they receive a wake-up message sent by the base station, they will be in active mode and start to measure the distances between the mobile tag and anchor nodes. The distances information will be then sent back to the base station for further processing. After these procedures, the mobile tag and anchor nodes will be again in sleep mode, until the next wake-up message comes. Figure 3.1 illustrates the communication procedure,

Step 1 the base station sends the wake-up message to wake up the mobile tag and anchor nodes.

Step 2 knowing the mobile tag and anchor nodes are awake, the base station sends to the mobile tag a ID-message, which contains the IDs of the anchor nodes that need to be connected with the mobile tag.

Step 3 the tag sends a blink-message to one specified anchor node, letting this node goes into active mode, and the rest waked up nodes stay in the stand-by mode.

Step 4 this active anchor node sends a poll-message to the mobile tag, containing the local sending timestamp.

Step 5 the mobile tag receives this poll-message, then sends out a respond-message. The receiving timestamp of the poll-message and the sending timestamp of the respond-message are recorded in the tag.

Step 6 the anchor node receives this respond-message, then sends out a final-message, containing the receiving timestamp of the respond-message and the sending timestamp of the final-message . Afterwards, the anchor node goes directly into sleep mode.

Step 7 the mobile tag receives this final-message, records the local receiving timestamp. Now the mobile tag has stored the timestamps of sending poll-message, receiving respond-message, sending final-message from the anchor node, and receiving poll-message, sending respond-message, receiving final-message from itself. With all this timestamps, the tag uses the DSTWR as mentioned in section 2.3, to calculate

its distance to this anchor node. And this distance will be stored as 'distance1' in its local memory.

Afterwards, the mobile tag will sends a blink-message to the second specified anchor node, and repeat the step 3 to 7 and stores 'distance2' and 'distance3' and so on, until all the nodes whose ID are listed in ID-message from step 2 has been communicated by the mobile tag.

Step 8 the mobile tag sends distance-message back to the base station, letting the base station to do the further data processing, for example distances calibration.

The above mentioned eight steps for one set distances measurement. Ideally, after each set measurement, the distances from mobile tag to all the anchor nodes are obtained. But in reality, due to signal interfering and hardware errors, some distances data will be missing.

Also note that, the messages sent between the mobile tag and the anchor nodes for distance measurements (step 3 to 6) are modulated with a high frequency UWB signal, which is different from the frequencies used for sending message from the base station. This can make sure the DSTWR procedure won't be disturbed by the incoming wake-up messages and ID-messages. However this alone can not prevent the DSTWR procedure of one node from being disturbed by the DSTWR procedure of other nodes, this will be explained later in section 3.2.
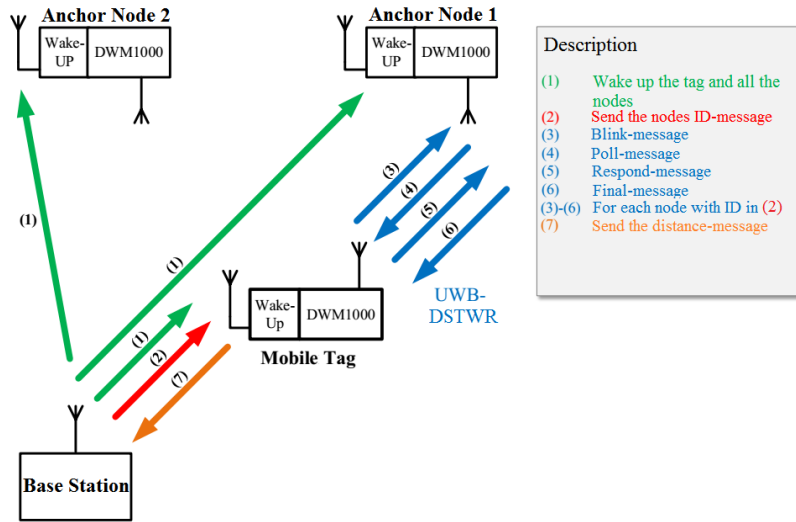
Figure 3.1: Procedure of communication between hardware for localization [12].

3.2 Modifications for Improvement Purpose

For getting a better system performance, modifications of the codes for the devices have been done, such as the timing issue, sleeping mode option and so on. Due to the limitation of the thesis length, not all the modifications are mentioned here.

Figure 3.2 shows the current consumption of one sampling cycle of the mobile tag before the system have been improved. As shown, this cycle starts from 150 ms and ends at 2800 ms, lasts for 2650 ms. Meanwhile, Figure 3.3 shows the current consumption of one sampling cycle of the mobile tag with improved implementation. As shown, this cycle starts from 150 ms and ends at 450 ms, lasts for 300 ms. This improvement has made the cycle 2350 ms shorter.
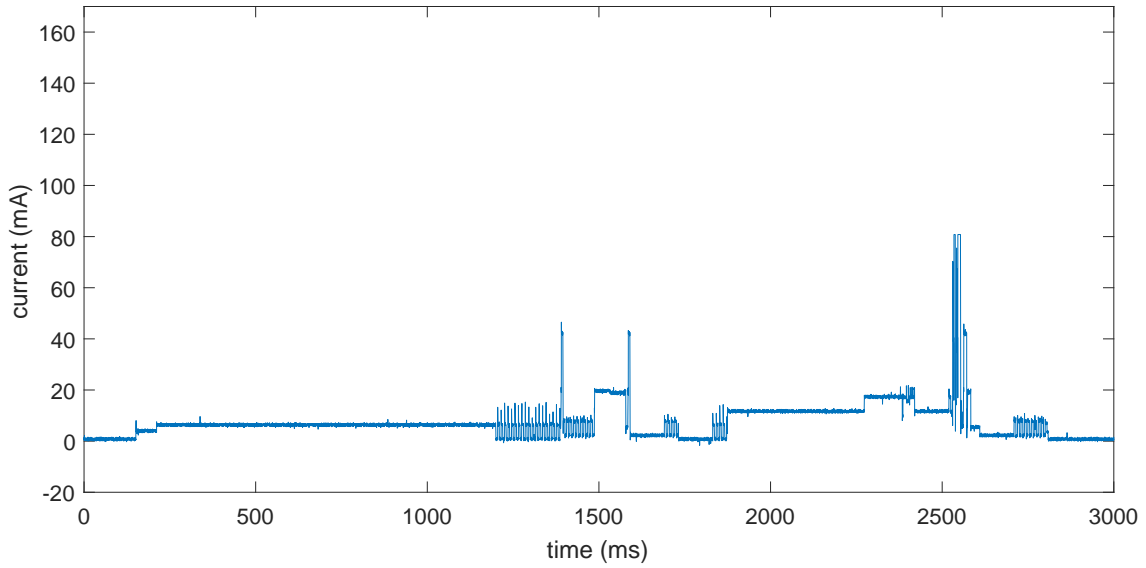
Figure 3.2: Oscilloscope: current consumption of one sampling cycle of tag, before improved.
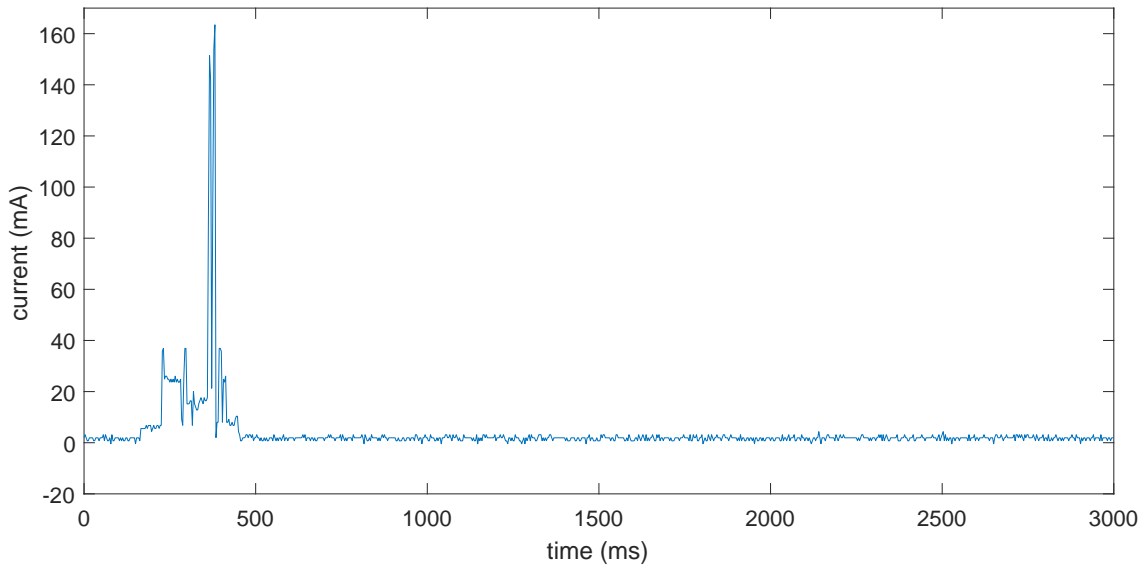
Figure 3.3: Oscilloscope: current consumption of one sampling cycle of the tag, after improved.

Figure 3.4 shows the process flow of the anchor nodes and mobile tag.
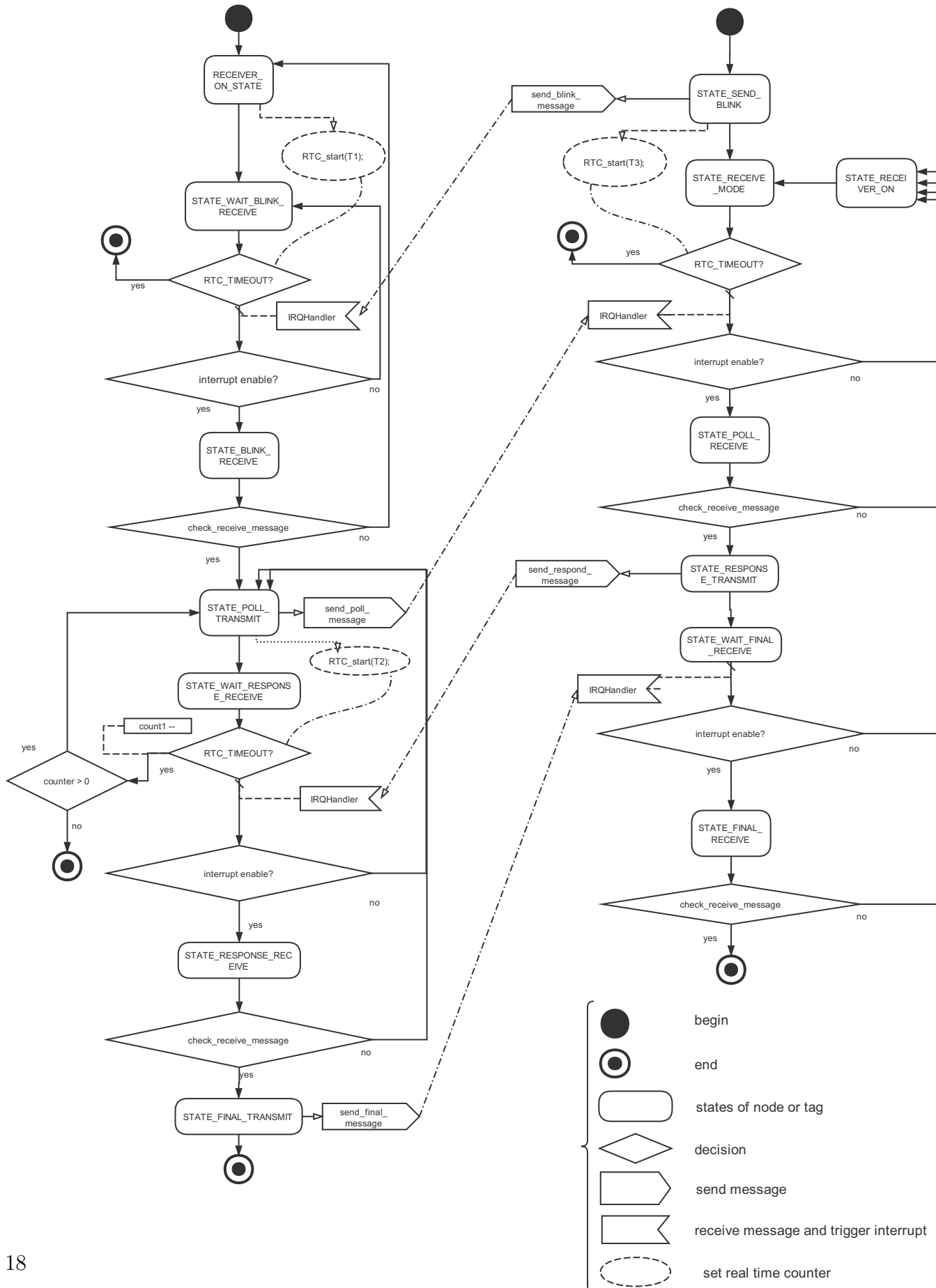
Figure 3.4: Simplified state machines of node and tag, upper left is state machine of node, upper right is state machines of tag, bottom right is the notations explanations.

18

Here, the communication procedure between tag and nodes is given as followed:

At the beginning, the tag sends a blink message at its state *state-send-blink*.

The node waits for this message after its state *state-wait-blink-receive*, and check the content of the message once it receives one. If the message contains the right information, i.e., the ID of this corresponding node, this nodes will go into a new state *state-poll-transmit* and send out a poll message. Here starts the DSTWR.

The tag checks for the received poll message, and send out the respond message.

The node checks for the received respond message, and send out the final message.

The tag receive the final message, calculates the distance, and finish the DSTWR. As mentioned in section 3.1.

The count-down looper for entering state *state-poll-transmit* in anchor node is vital for the case when more than one nodes are used. Since all the poll, respond and final message are carried by signal with the same frequency, if two of the anchor nodes are in the states *state-poll-transmit* or *state-wait-blink-receive*, this will leads to the case where, these nodes received poll message from each other, and go back to *state-poll-transmit* and send poll message again and again, as illustrated in Figure 3.5. Because what they are expecting is the respond message from the tag, the poll message from the other node can not pass the checking step. The above mentioned unwanted communication can be detected by checking the current consumption of the anchor node, as the repeating peaks showed in Figure 3.6. While the current consumption of a normal measurement cycle as illustrated in Figure 3.7. By comparing these two figures, we can also notice the time consumption for a measurement cycle have a 4 second different.
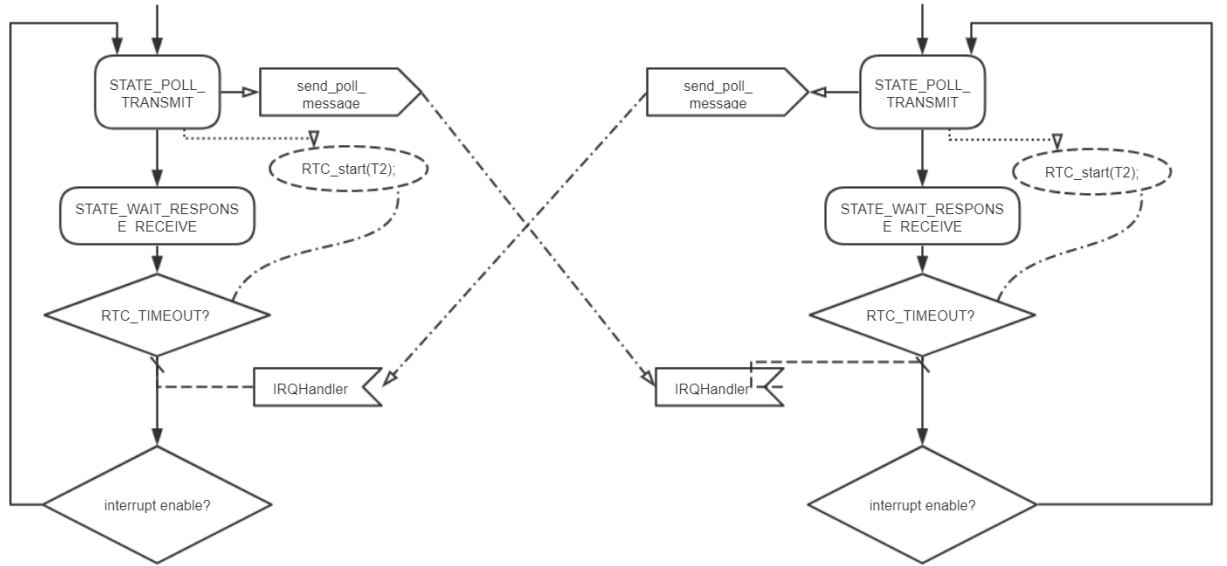
Figure 3.5: Unwanted communication happens, nodes receive other node's poll message, while they are expecting respond message from the tag. This happens when the tag has started communicating with the next node, while the last node missed its respond message and is still waiting for it.
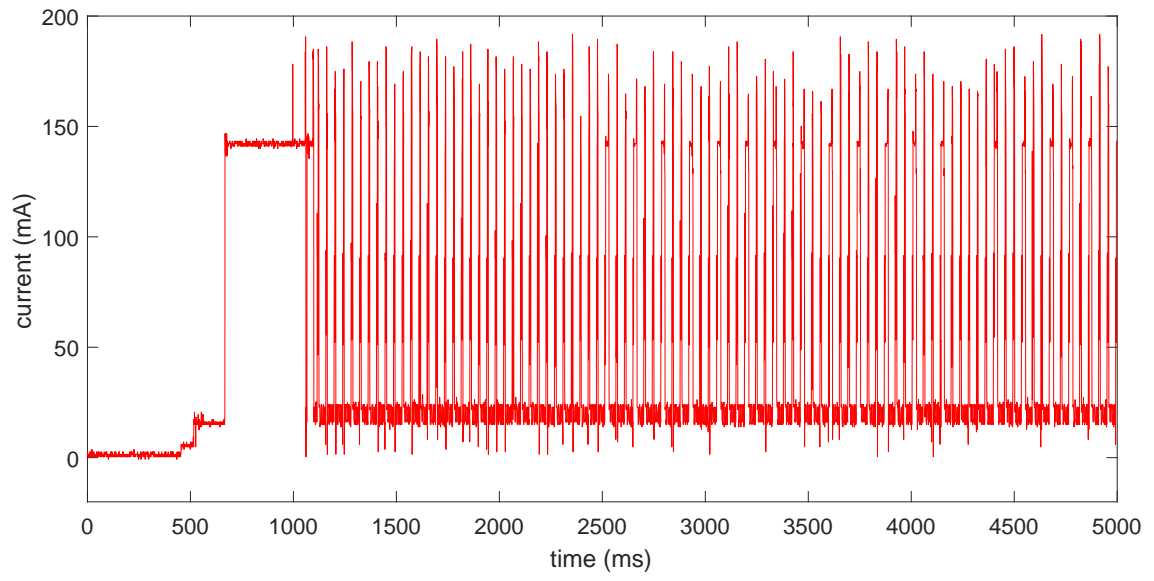
Figure 3.6: Oscilloscope: current consumption of one node when repeating communication between nodes happens.
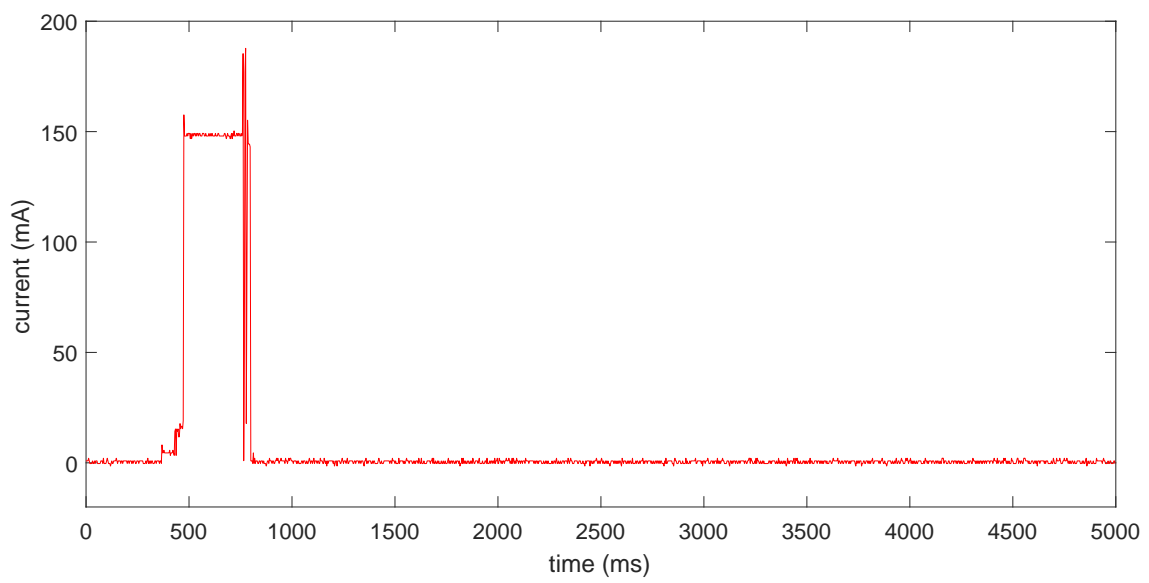
Figure 3.7: Oscilloscope: current consumption of node, one sampling cycles in normal cases.

Besides from the count-down loop above, the properly tuned waiting time of each real time counters in Figure 3.4 can also help to reduce to rate of occurrence of the unwanted communication. The basic principle behind is try to keep the measurement of the tag longer than the one of the nodes, so that the tag won't start to communicate with other node too soon. The optimal waiting time for the RTCs for this thesis are list in Table 3.1,

Table 3.1: Optimally tuned waiting time (ms) for the RTCs in Figure 3.4

RTC	T1	T2	T3
time	800	30	110

In Figure 3.4, some real time counters (RTC) are set to prevent the tag and node from waiting in one state when the message was not received or when the message received could not pass the checking step. Besides, this RTCs need to realize the functionality of making sure the tag must not communicate with two nodes and the same time, with the same reason mentioned above.

3.3 Improvement Results

In this subsection, two quantifiable characteristics are chosen as the system's evaluation indicators for performance comparison, namely, the *sampling rate* and the *measurements obtained rate.*

The *sampling rate* indicates how fast the system can obtain the distances between the mobile tag and the anchor nodes. It is obvious that the greater the *sampling rate* is, the higher resolution of the trajectory of tag can be obtained by the system.

The *measurements obtained rate* is defined as the ratio of the actually number of obtained measurements to the expected number of measurements. In ideal cases, where no measurements are missing, the measurements obtained rate should equal to 1. However, due to the reasons as explained in section 3.2, distance information to some nodes can not be obtained in reality. The greater the the *measurements obtained rate* is, the more information about the trajectory of tag and the position of anchor nodes can be obtained by the system.

From the experiments done with system before and after improvement, 4 sets of data are selected randomly for this comparison. Each set of data contains the distances from the mobile tag to 5 anchor nodes, and the time stamps when these measurements are done.

3.3.1 Sampling Rate

To obtain the maximal sampling rate, the mobile tag needs to be operated incessantly, which means that the tag needs to be waked up immediately after going to sleep. To ensure this, during the experiment, the base station sends out wake-up messages and the ID message at relatively high rate, $10Hz$, which is sufficient since

the maximal measurement sampling rate of the system is only $2Hz$ as determined in later experiments. A terminal program for serial communication, 'Hterm' [24] is used to read distance information from base station and to send command instructions to the base station. The instructions include when and in which frequency to send out the wake-up messages and ID-messages.

Figure 3.8 shows the normalized histogram of time interval between the time stamps of measurements in 4 experiments done with the system before and after improvements. Among those experiments before improvements, 99 sets of measurements value, i.e. 99 time stamps are recorded and $99 \cdot 5 = 495$ distance value are expected, when using 5 anchor nodes. The achieved shortest time interval value is $1.2010\ s$ while the average time interval is $2.8276\ s$. Among those experiments after improvements, 1106 sets of data are recorded, i.e. 1106 time stamps are obtained and $1106 \cdot 5 = 5530$ distances are expected. The achieved shortest time interval value is $0.4690\ s$. The average value of time intervals is $0.6753\ s$. Table 3.2 shows the minimal and the average value of the time interval recorded in these experiments before and after system improvements.
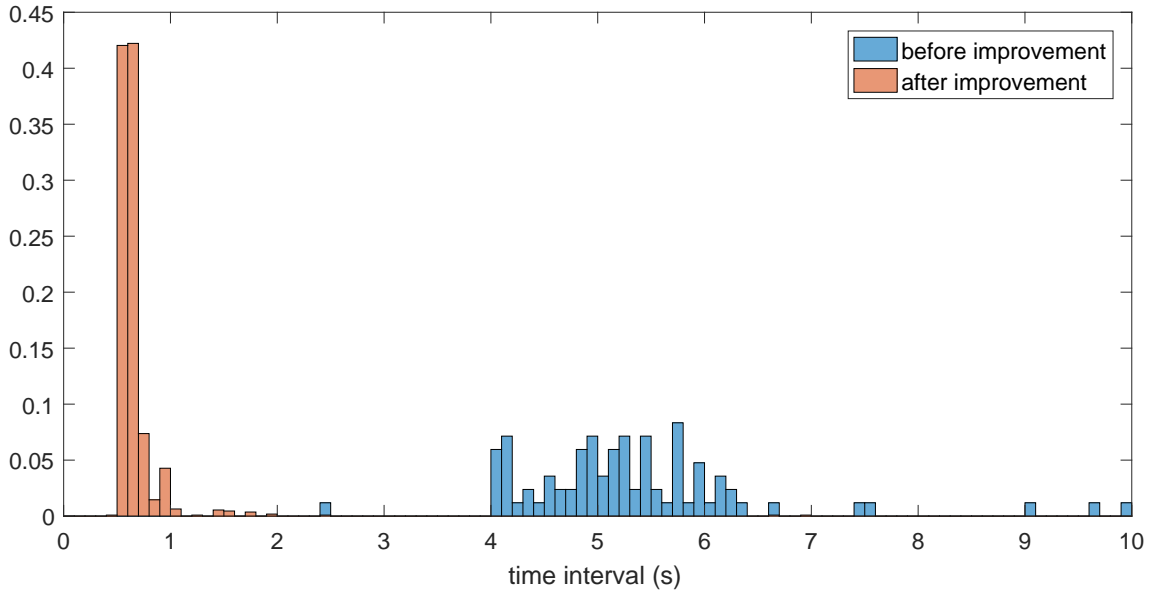
Figure 3.8: Normalized histogram of time interval between stamps from experiments (4 experiments have been made before and after system improvement).

Although the shortest time interval value obtained is $1.2010s$ and $0.4690s$ respectively by the system before and after improvement, these values are rarely occurred. So the average values, namely 2.8276 and 0.6753 are better indication for calculating the sampling rate. The sampling rate before system improvement f_{before} is

$$f_{before} = \frac{1}{2.8276second} = 0.3537Hz. \tag{3.1}$$

And the sampling rate after system improvement f_{after} is

$$f_{after} = \frac{1}{0.6753 second} = 1.4808 Hz. \tag{3.2}$$

Based on the value from Equation 3.1 and Equation 3.2, the sampling rate has been improved from **0.3537Hz** to **1.4808Hz**, i.e., increased by more than **4** times.

Table 3.2: Minima and mean value of the time interval, before and after system improved (in second)

BEFORE	exp 1	exp 2	exp 3	exp 4
min	2.0670	2.0200	2.0659	1.2010
mean	2.9040	2.6034	2.5941	3.1767
AFTER	**exp 1**	**exp 2**	**exp 3**	**exp 4**
min	0.5310	0.4690	0.5010	0.5320
mean	0.6856	0.7195	0.6598	0.6599

3.3.2 Measurements Obtained Rate

Due to interfering or timing issue as described in section 3.2, sometimes measurement is missing. The number of received measurements within each measurements set can vary from 0 to N, where N is the total number of nodes in used. Measurements obtained rate can be considered from two aspects.

One aspect to consider the measurements obtained rate is the **total measurements obtained rate** r_{total}, which is defined as the ratio of the number of received measurements in total $m_{received}$ to the number of expected measurements in total $m_{expected}$ within an experiment, as shown in Equation 3.3.

$$r_{total} = \frac{m_{received}}{m_{expected}} \tag{3.3}$$

Table 3.3: Values of total measurements obtained rate before and after system improvement

	before improvement	after improvement
r_{total}	0.463	0.842

Based on the experiments data sets as the ones used in subsection 3.3.1, r_{total} of the system before and after improvement have been calculated and have the values as listed in Table 3.3. Before system improvement, r_{total} has the value of 0.463, which means that more than half of measurements were missing during experiments before improvement. In comparison, after system improvement, r_{total} is 0.842, which is almost double the value as before. The increase of the r_{total} is an indication that the sampling procedure of the ranging system is more effective and can obtained more information about the trajectory of the moving target.

Another aspect to consider the measurements obtained rate is the **occurrence rate** r_n of n valid measurements, n varies from 0 to N, where N is the total number

of anchor nodes in used. r_n is defined as the ratio of the number of times s_n that only n measurements are received in one measurements sets, to the total number s_{total} of measurements sets, as shown in Equation 3.4. Since at least measurements to at least three anchor nodes are needed to determine the position of the mobile tag, measurements sets that contain less than three measurements would be treated as invalid measurements sets. For this reason, as 5 anchor nodes are used in our experiments, we require a system which has big values for *occurrence rate* r_3, r_4 and r_5, while values for its r_0, r_1 and r_2 are small.

$$r_n = \frac{s_n}{s_{total}} \tag{3.4}$$
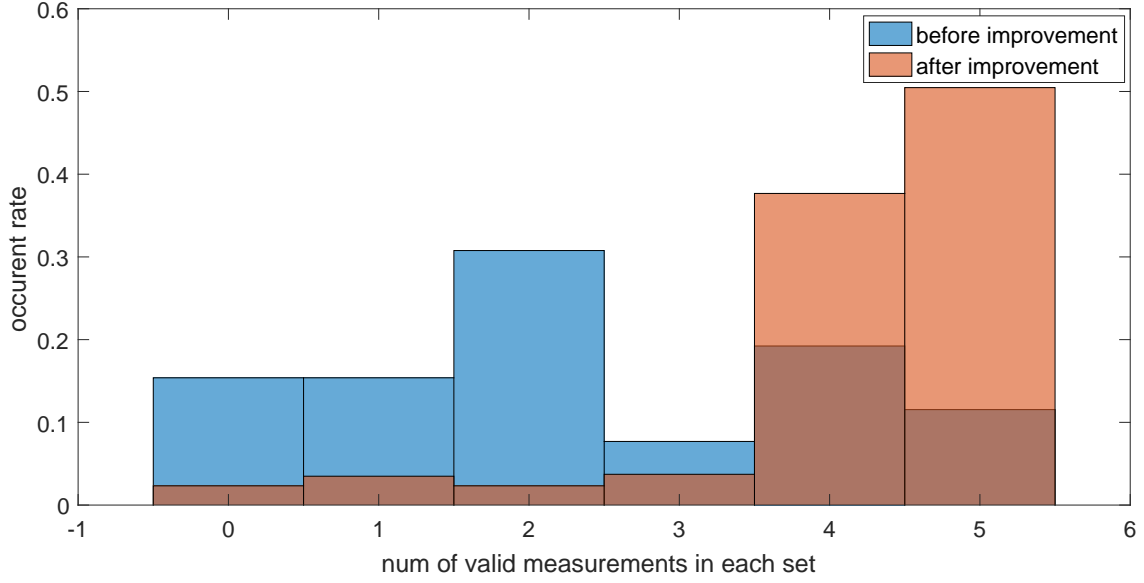
Figure 3.9: Normalized histograms of occurrence rate r_n, before and after system improvement.

Based on the same data sets, the normalized histograms of r_n are plotted as shown in Figure 3.9. It is easy to recognized that, the occurrence rate of 4 and 5 measurements are higher after system improvement, while occurrence rate of 0, 1 and 2 are lower. These can be a good indication that the system performance has been significantly improved. As the occurrence rates of invalid measurements set decreased and the occurrence rates of valid measurements set increased, we can see the noteworthy improvement of the system performance.

For a better comparison, the Table 3.4 shows the values of measurement obtained rates, where the occurrence rate of 5 measurements increases from 0.115 to 0.50, the occurrence rate of 4 measurements increases from 0.190 to 0.38. Meanwhile the occurrence rate of 3 measurements decreases from 0.075 to 0.035, the occurrence rate of 2 measurements decreases from 0.310 to 0.025, the occurrence rate of 1 measurements decreases from 0.155 to 0.035, the occurrence rate of 0 measurements decreases from 0.155 to 0.025.

Table 3.4: Measurements obtained rate of n distance value in one measurement

	n=0	n=1	n=2	n=3	n=4	n=5
before	0.155	0.155	0.310	0.075	0.190	0.115
after	0.025	0.035	0.025	0.035	0.380	0.500

With the increased sampling rate and data obtained rate, the new system are now able to localize a moving target with a human walking speed.

In the next chapters, three different algorithms were built to calculate the trajectory using the collected distance data. Based on the trajectory results, the performance of the improved system is evaluated.

4 System Measurement Calibration

In this chapter, the system calibration procedure is explained and the calibration results are discussed.

The distance measurement performs linearly when the distance is longer than 2 m [12]. In which case, the linear relation between the distance measurement value d_{meas} and the true distance d_{true} can be expressed as Equation 4.1,

$$d_{meas} = a_1 \cdot d_{true} + a_2 \tag{4.1}$$

where a_1 and a_2 are the system parameters to be determined. These two parameters depend greatly on the system, i.e. the tag and the node. Since there is only one tag being in use, a_1 and a_2 only depend on each node respectively. When the distance is shorter than 2 m, the relation between d_{meas} and d_{true} is polynomial [12].

This section presents how to determine a_1 and a_2 for each node.

4.1 Calibrations Setup

The data for system calibration is collected in the grass field far away from buildings. Such experiment environment can reduce the occurrence rate of multipath propagation, caused by the signal reflections from walls and metals. Meanwhile, to reduce the reflections from the ground, the tag and the nodes are placed on the top of wooden sticks of 1.3 m. The setup is shown in Figure 4.1.
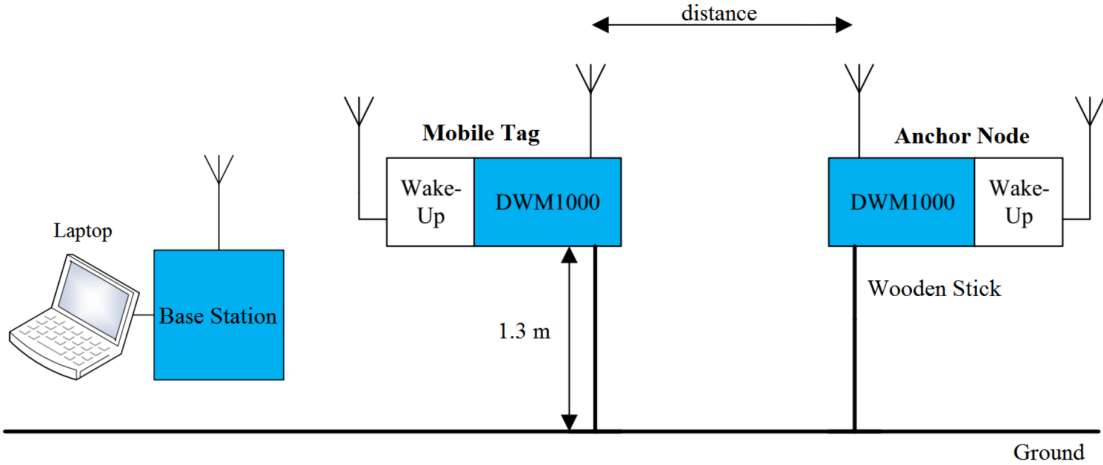
Figure 4.1: Schematic of setup for calibration.

4.2 Calibrations Results

The values for d_{true}, i.e. the distances between the tag and each node, have been chosen as 3, 4, 5, 6, 8m. For each d_{true} value, 500 measurements have been obtained for each node. Due to the existence of the outliers among the measurement data, when calculating the mean values and the variances of these measurements, the highest and lowest 5% of data are treated as outliers and have been excluded. Then, the mean values and variances of the measurements are listed as Table 4.1 and Table 4.2. The mean values shown in Table 4.1 are denoted as the values for d_{meas} in Equation 4.1. For each node, there are 5 pairs of $\{d_{meas}, d_{true}\}$ value. With these 5 pairs value, linear least squares fitting is applied to determine the values for a_1 and a_2 of each nodes. Table 4.3 shows the optimal value for a_1 and a_2 after linear fitting. Figure 4.2 shows the linear fitting of the measurements of one the the nodes. The fitting line fits the data with a RMSE of 135.3 mm. The fittings of the other nodes have the similar results.

Table 4.1: Mean of measurements of each node (mm), when placed 3m, 4m, 5m, 6m and 8m away from the tag.

node ID \ d_{true}	3000	4000	5000	6000	8000
0x1	3274	4701	5407	6566	8048
0x2	3337	4308	5137	6208	8390
0x3	3158	4237	5428	6453	8251
0x4	3187	4300	5367	6237	8135
0x5	3445	4702	5582	6282	8132

Table 4.2: Mean absolute deviation of measurements of each node (mm), when placed 3m, 4m, 5m, 6m and 8m away from the tag.

node ID \ d_{true}	3000	4000	5000	6000	8000
0x1	13.79	19.79	23.58	32.87	36.31
0x2	14.78	28.31	20.16	24.99	60.55
0x3	35.24	17.65	23.15	27.23	38.23
0x4	27.32	24.95	23.81	19.61	43.83
0x5	16.56	36.95	19.86	17.24	28.50

The deviations value in Table 4.2 are used to determined the value of the measurements noise matrix $\mathbf{R}$ in the EKF algorithm. One can use a polynomial function to fit these data, so that for any distance to each node there will be a determined value as deviation. And the square of this deviation is served as the corresponding diagonal entry of $\mathbf{R}$. However, this will lead to high computational consumption. To avoid this, for each node we simply tread the mean values of the 5 deviations

as the deviation for all distances. By doing so, we obtained the deviation σ_i of measurement of node i as listed in Table 4.4.

Table 4.3: Optimal value for system parameters after linear fitting

node ID	a_1	a_2 (mm)
0x1	1.052	-688
0x2	0.989	-218
0x3	0.973	-159
0x4	1.017	-339
0x5	1.074	-796

Table 4.4: Standard deviation of measurements of nodes (mm)

σ_1	24.7055
σ_2	29.7639
σ_3	28.3065
σ_4	27.9094
σ_5	21.6547
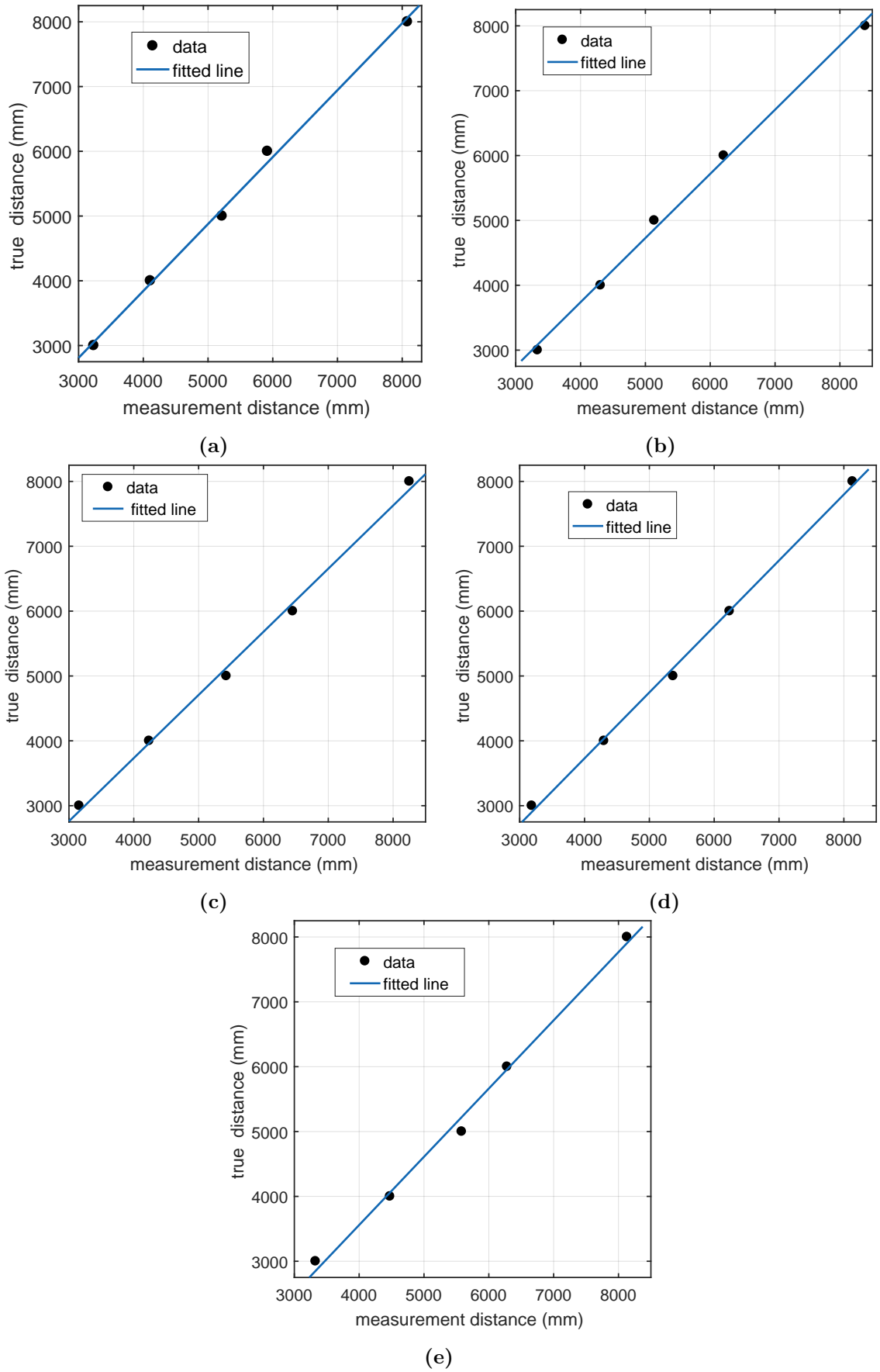
Figure 4.2: Linear fitting of measurements of nodes. (a)0x1, (b)0x2, (c)0x3, (d)0x4, (e)0x5.

4.3 Data Analysis

This subsection discusses the distributions of the obtained data.

Theoretically, the distributions of the measurement data with one fix distance of one node should follow normal distribution.

Figure 4.3 shows some of the histograms of measurements value in real world experiments. The true distance is 4 meters and around 500 measurements are obtained for each node. The red curves in the same figures represent the Gaussian distributions that best fit the histograms. The red curves are generated by MAT-LAB function 'histfit', which fits a normal density function to the histogram. As can be seen, not all the distributions are gaussian. In fact, the *Lilliefors test* rejects the hypothesis that the measurements data of node '0x1' and '0x3' is Gaussian distributed as shown in subplots Figure 4.3a and Figure 4.3c. *Lilliefors test* is a normality test. It is used to test for hypothesis that data come from a Gaussian distributed population [25] [26]. The subplots Figure 4.3d and the Figure 4.3e follow Gaussian distribution, the variance of the data can be explained as the result caused by the system and environmental random noises. Figure 4.3a, Figure 4.3b and Figure 4.3c contain heavy tail at the end, which might be cased by the multipath propagation.
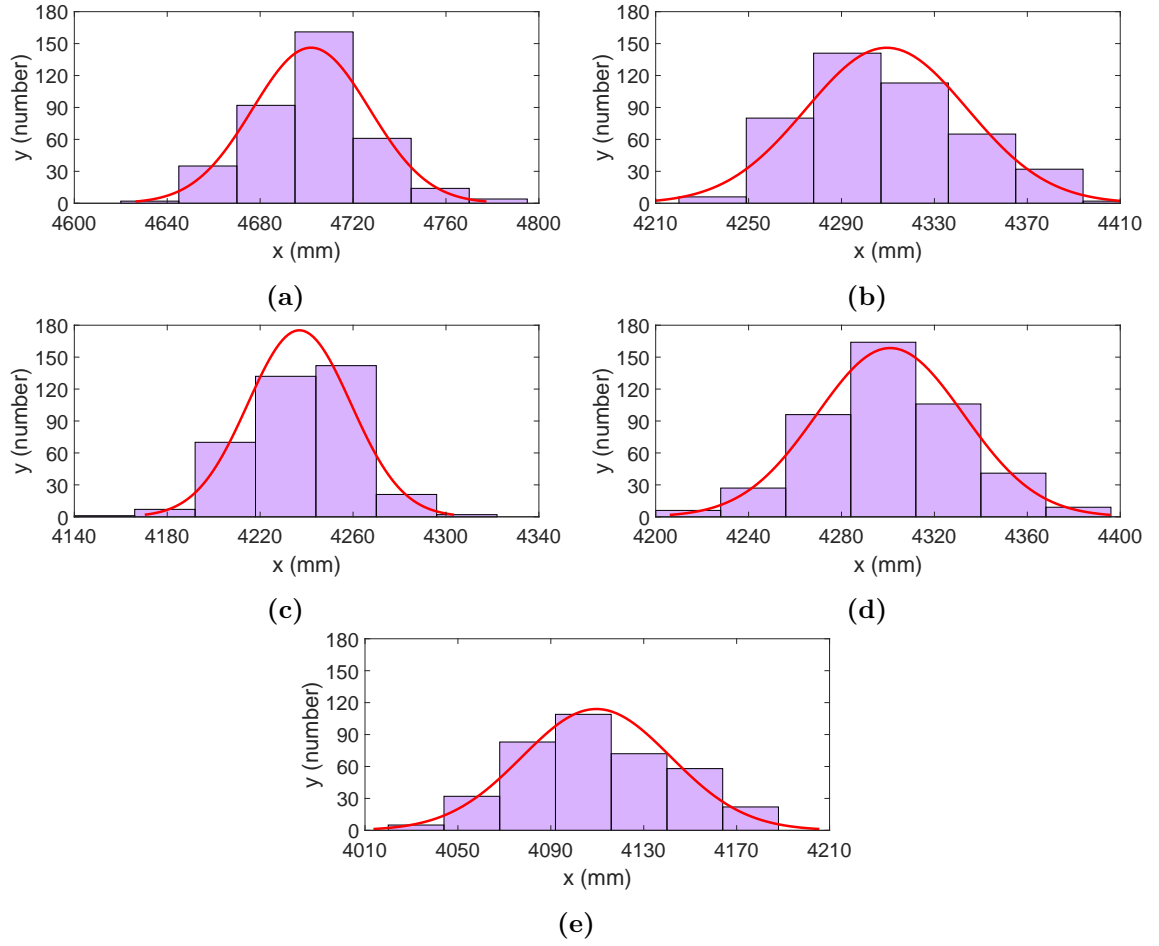
Figure 4.3: Histograms of d_{meas} of different nodes, when d_{true} is 4 meters.

5 Localization Algorithms

In this chapter, three localization algorithms based on EKF and OM were built and explained. Among these algorithms, two are based on EKF and one is based on OM. The two algorithms based on EKF use different measurements combinations (MC) within one measurements set for observation update. The EKF using Measurements Combination 1 (EKF-MC1) treats a whole measurements set as one observation, and updates each time with all the measurements within this measurements set. While the EKF using Measurements Combination 2 (EKF-MC2) treats every single valid measurement within a measurements set as one observation, and updates n times with every measurement within this measurements set, where n is the number of valid measurements of the measurements set.

5.1 EKF using Measurements Combination 1

Consider the case in a two dimensional space, the state vector $\mathbf{x}$ of the target, i.e. the mobile tag, contains its positions p_x, p_y and the velocities $\dot{p}_x$, $\dot{p}_y$, in which the subscript x and y indicate their components in x- and y-axes of a Cartesian coordinate system.

$$\mathbf{x} = [p_x, p_y, \dot{p}_x, \dot{p}_y]^T \tag{5.1}$$

State Transition Modelling

For the transition model, random walk models [27] is used in this thesis. In a random walk model, the velocity of the mobile tag is assumed to be constant before the next estimation. The state transition model can be illustrated in a mathematical way as Equation 5.2,

$$\mathbf{x}_k = \mathbf{A} \cdot \mathbf{x}_{k-1} + \mathbf{G} \cdot \mathbf{w}_k = \begin{bmatrix} 1 & 0 & dt & 0 \\ 0 & 1 & 0 & dt \\ 0 & 0 & 1 & 0 \\ 0 & 0 & 0 & 1 \end{bmatrix} \cdot \mathbf{x}_{k-1} + \begin{bmatrix} \frac{1}{2} \cdot dt^2 & 0 \\ 0 & \frac{1}{2} \cdot dt^2 \\ dt & 0 \\ 0 & dt \end{bmatrix} \cdot \begin{bmatrix} \ddot{p}_x \\ \ddot{p}_y \end{bmatrix} \tag{5.2}$$

where noise are treated as the accelerations of the mobile tag $\ddot{p}_x$ and $\ddot{p}_y$ in the $x-$ and $y-$axes.

The Equation 5.2 is the concrete form of Equation 2.17, where $\mathbf{u}_k$ is $\mathbf{0}$, and the $f(\cdot)$ is described as a linear matrix multiplication as the same as $\mathbf{A}$ in Equation 2.9,

The accelerations $\ddot{p}_x$ and $\ddot{p}_y$ are assumed to be independently distributed random values, making the process noise $\mathbf{w}_k$ has the form of followed,

$$\mathbf{w}_k = \begin{bmatrix} \ddot{p}_x \\ \ddot{p}_y \end{bmatrix}. \tag{5.3}$$

Thus the $\mathbf{Q}_k$ in Equation 2.20 into concrete form as followed,

$$\mathbf{Q}_k = \mathbf{G} \cdot \mathbf{w}_k \cdot \mathbf{w}_k{}^T \cdot \mathbf{G}^T = \begin{bmatrix} \frac{1}{2} \cdot dt^2 & 0 \\ 0 & \frac{1}{2} \cdot dt^2 \\ dt & 0 \\ 0 & dt \end{bmatrix} \cdot \begin{bmatrix} \ddot{p}_x \\ \ddot{p}_y \end{bmatrix} \cdot \begin{bmatrix} \ddot{p}_x \\ \ddot{p}_y \end{bmatrix}^T \cdot \begin{bmatrix} \frac{1}{2} \cdot dt^2 & 0 \\ 0 & \frac{1}{2} \cdot dt^2 \\ dt & 0 \\ 0 & dt \end{bmatrix}^T \tag{5.4}$$

Observation Modelling

The observation model maps the observation space into the state space, interpreting the relation between the state vector $\mathbf{x}$ and its observation $\mathbf{z}$. Assume the state vector $\mathbf{x}_k$ at current time step is $[p_x, p_y, \dot{p}_x, \dot{p}_y]^T$ and one of the anchor nodes i is located in known position $[n_{ix}, n_{iy}]^T$. The observation $\mathbf{z}_i$ of node i, i.e., the distance between the mobile tag and this anchor node , can be calculated as Equation 5.5. Thus the observation model function is as shown in Equation 5.6.

$$\mathbf{z}_i = \sqrt{(n_{ix} - p_x)^2 + (n_{iy} - p_y)^2} \tag{5.5}$$

Equation 5.6 is the concrete form of Equation 2.18, only without the noise term $\mathbf{v}_k$. Note that Equation 5.5 is a nonlinear function, which is impossible to be processed in a KF. To use EKF, Equation 5.6 should be linearized as in Equation 2.26, which makes the observation matrix $\mathbf{H}$ has the form as illustrated in Equation 5.7.

$$h(\mathbf{x}) = (\mathbf{z}_1, \mathbf{z}_2, ..., \mathbf{z}_i, ...)^T \tag{5.6}$$

$$\mathbf{H} = \left.\frac{\partial h}{\partial \mathbf{x}}\right|_{\mathbf{x}_k} = \begin{bmatrix} \frac{p_x - n_{1x}}{\sqrt{(n_{1x}-p_x)^2+(n_{1y}-p_y)^2}} & \frac{p_y - n_{1y}}{\sqrt{(n_{1x}-p_x)^2+(n_{1y}-p_y)^2}} & 0 & 0 \\ \vdots & \vdots & \vdots & \vdots \\ \frac{p_x - n_{ix}}{\sqrt{(n_{ix}-p_x)^2+(n_{iy}-p_y)^2}} & \frac{p_y - n_{iy}}{\sqrt{(n_{ix}-p_x)^2+(n_{iy}-p_y)^2}} & 0 & 0 \\ \vdots & \vdots & \vdots & \vdots \end{bmatrix} \tag{5.7}$$

For the covariance of observation noise $\mathbf{R}_k$, this thesis assumes it is constant and the observations to each anchor nodes are independent, so $\mathbf{R}_k$ can be assumed as a diagonal matrix, with the variance σ_i of each anchor node measurements as the main diagonal entries,

$$\mathbf{R}_k = \mathbf{R} = \begin{bmatrix} \sigma_1^2 & 0 & ... & 0 \\ 0 & \sigma_2^2 & ... & 0 \\ \vdots & \vdots & \ddots & \vdots \\ 0 & 0 & ... & \sigma_i^2 \end{bmatrix} \qquad (5.8)$$

the way how σ_i is determined has been described in section 4.2, and the value of σ_i are listed in Table 4.4.

In EKF-MC1 of EKF, all the valid distance measurements within one measurement set are considered as one single observation for the EKF correction step. Since there are 5 anchor nodes in use, each observation contains 0 to 5 valid distances (as discussed above, distance values smaller than 2 m are consider as invalid). When one observation contains invalid distance measurements, the correction step would be skipped in this EKF update.

5.2 EKF using Measurements Combination 2

As mentioned in section 3.1, when the system measure distances between tag and nodes, the tag can only communicate with one node each time, instead of communicating with all the nodes at the same time. This means that even within one sampling cycle, the distances to different nodes are not measured at the same time. In fact, there is a 30 ms time gap between each two measurements within one measurements set, which can be observed from the oscilloscope in the current-time plot of the tag, as shown in Figure 5.1.

One way to treat this 30 ms time gap is to ignore it, since it is relatively very small compare to one sampling cycle (about 500 ms), as shown in Figure 5.1. So in each EKF update cycle, all the 5 measurements in one measurements set are treated as measured at the same time. This leads to the EKF using Measurements Combination 1 (EKF-MC1) in section 5.1.

Another way to treat these 30 ms time gaps is the opposite. Assume that the tag is moving in a fast speed, for example 10 m/s, within one measurement cycle, the time gap between the measurements from the last node to the first node is calculated as $(5-1) \cdot 30 \ ms = 120 \ ms$, within which the tag can have a displacement of $0.12 \cdot 10 = 1.2 \ m$. It is obvious improper to treat this points as close to each other. One way to solve this situation is to treat each one of the five measurements as an individual observation for each EKF update. So, instead of updating EKF once using all five measurements within one set, the EKF is updated 5 times with each measurement to one of the five nodes at a time. In the scope of this thesis, this implementation of EKF is called EKF using Measurements Combination 2 (EKF-MC2).

As described in section 3.1, for each set of measurements, all the 5 distances value are sent back to the base station in one package, so the station can only generate one time stamp $t_{package}$ for receiving this package. However, based on the Current-Time
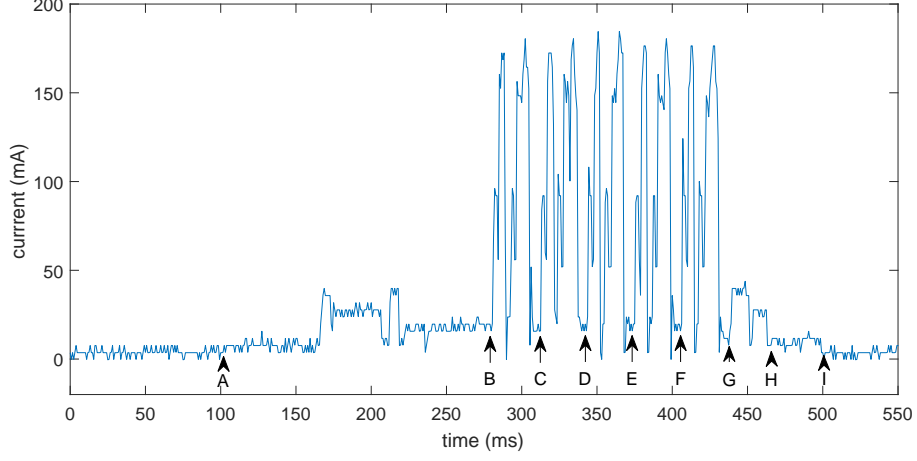
Figure 5.1: Current-time plot of tag, one measurements set of 5 measurements. A and I are the starting and end points. Section AB is the preparation period. BC, CD, DE, EF, FG are the periods when communicating with first, second, third, forth, fifth node. GH is the periods for sending the distances message to the base station.

plot of one sampling cycle of the tag as shown in Figure 5.1, we can observe that, the communication time between tag and each node is about 30 ms. The distance to the $5th$ node is measured at time stamp 'G', about 30 ms before $t_{package}$, which is marked as 'H'. Here, we assume the time stamp of sending the package in the mobile tag is equal to the time stamp of receiving the package in base station, since the distance between tag and base station is only 2 to 5 m. Likewise, the distance to the $4th$, $3th$, $2nd$, $1st$ nodes are generated at time stamps $t_{package} - 60$ ms, $t_{package} - 90$ ms, $t_{package} - 120$ ms, $t_{package} - 150$ ms. With these time stamps, the time interval between each two adjacent EKF update can be determined. The process of EKF update is shown in Figure 5.2, where the gray curves are the same trajectories of the tag. Crosses donate the time when the measurements to different nodes are taken. Red crosses donate the points when EKF observation updates are taken.

Figure 5.2: EKF updates, upper is the estimations of EKF-MC1, bottom is EKF-MC2. The gray curves are the true trajectories. Crosses donate the time when the measurements to different nodes are taken. Red crosses donate the points when EKF observation updates are taken. Δt equals to $30ms$.

36

5.3 Optimization Method for Localization

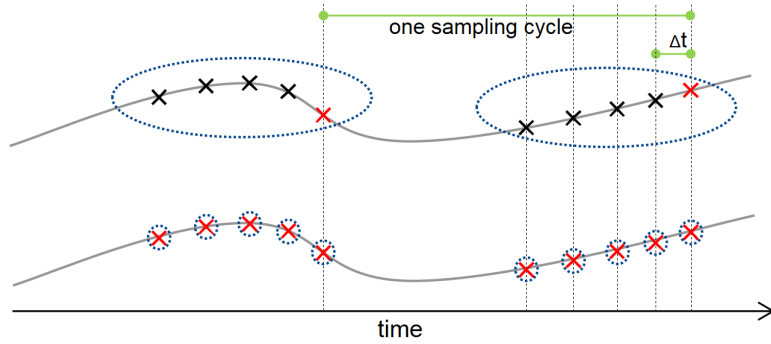The aim of Optimization Method (OM) for localization is to localize the anchor nodes and the mobile tag simultaneously. This algorithm doesn't require the pre-knowledge of all the positions of the anchor nodes, thus is suitable for the case, when not all the positions of the anchor nodes can be easily determined.

The principle of this algorithm is demonstrated as followed: the positions of the tag and nodes are estimated by applying an optimization method based on purely distance measurements data. Since no specific positions of any of these points are given, this estimated positions can only be optimized in a floating coordinate frame. To transform this floating coordinate frame into the desired coordinate frame, the true positions of at least 3 nodes in the global coordinate frame are required. The transformation matrix can also be determined with optimization methods [28].

We now consider the task of localization in two dimensional Euclidean space. It is assumed that, there is no mirror symmetry between the positions of nodes. The ranging network consists of n anchor nodes and the trajectory of the mobile tag consist of m discrete positions. This leads to $2n + 2m$ variables in two dimensional Euclidean space. Assuming all the distances measurements between each m positions of tag and n nodes have been obtained, we have $n \cdot m$ known value. The degree of freedom M of this localization problem can be calculated as Equation 5.9. When $M(n, m) > 0$, the problem is under-determined. When $M(n, m) = 0$, there should be a unique solution. When $M(n, m) < 0$, the problem is over-determined. When the problem is not under-determined, optimization methods can be applied to solved for these $2n + 2m$ variables, such gradient descent and Gauss-Newton algorithm. Gradient descent is an optimization method to find a minimum of a function, by iteratively taking steps proportional to the negative of the gradient of the function at the current point. And Gauss-Newton method consists of a sequence of linear least squares approximations to the nonlinear problem, each of these approximations is solved by an iterative process [29].

The optimization problem can be formulated as Equation 5.10 and Equation 5.11, where $\mathbf{n}_i$ and $\mathbf{m}_j$ are the estimated positions of node i and tag' trajectory point j, d_{ij} is the measured distance between node i and tag point j, $\|\cdot\|$ is the euclidean distance.

After the positions are determined in the floating coordinate frame by solving Equation 5.10, transformation matrix will be apply to these positions to transform them into the global coordinate frame.

$$M(n, m) = 2n + 2m - n \cdot m \tag{5.9}$$

$$\arg \min \sum_{i=1}^{n} \sum_{j=1}^{m} (f_{ij})^2 \tag{5.10}$$

$$f_{ij} = \|\mathbf{n}_i - \mathbf{m}_j\| - d_{ij} \tag{5.11}$$

In this thesis, the Levenberg-Marquardt algorithm are chosen as the optimization methods for solving the above mentioned problems. The Levenberg-Marquardt algorithm is a combination of the gradient descent method and the Gauss-Newton method [30]. Since the number of anchor nodes n is 5 , in order to make the sure $M \leqslant 0$ in Equation 5.9, the number of the tag's trajectory points m must hold $m \geqslant 4$.

5.4 Measurement Outliers Mitigation

In this section, a measurement outliers mitigation algorithm that works with EKF-MC1 is explained. For the following part of the thesis, this algorithm is called as Linear Weighted Combination based on Residual (EKF-LWCR).

The residuals are defined as the measurement residuals, i.e. the difference between the true observations (the obtained measurements data) and the estimated observations, as shown in Equation 5.12. Its detail explanation has been illustrated in section 2.4.

$$\mathbf{r} = \mathbf{z}_k - \mathbf{H}\hat{\mathbf{x}}_k^- \tag{5.12}$$

For the observation update at time step k, we assume that this observation contains n ($n \geqslant 3$) measurements, the number of combinations of measurements that can localize the mobile tag, denoted as $|C|$, can be calculated as Equation 5.13.

$$|C| = \sum_{i=3}^{n} \binom{n}{i} \tag{5.13}$$

For example, if one observation contains 5 measurements. To localize the mobile tag, we can select 3, 4 or 5 out of these 5 measurements as valid measurements combinations. Thus the value of N_{com} in this case is 16, as calculated in Equation 5.14.

$$|C| = \binom{5}{3} + \binom{5}{4} + \binom{5}{5} = 10 + 5 + 1 = 16. \tag{5.14}$$

.

Using each measurements combination C_i of these $|C|$ combinations for EKF observation update, different intermediate state estimation $(\mathbf{x}_{ki}, \mathbf{P}_{ki})$ can be obtained, thus $|C|$ intermediate state estimations in total.

To obtained the final state estimation, the linear weighted combination should be applied to these $|C|$ intermediate state estimations. The weight w_i of the intermediate state estimation is calculated as the normalized sum of the residual squares, as shown in Equation 5.15,

$$w_i = \frac{\sum_{j \in C_i} (r_j)^2}{|C_i|} \tag{5.15}$$

.

where j denotes the jth measurements in the combination C_i, r_j is the corresponding j^{th} residual of $\mathbf{r}$, $|C_i|$ is the number of measurements in this combination.

So the final state estimation can be calculated as shown in Equation 5.16 and Equation 5.17

$$\mathbf{x}_k = \frac{\sum_{i=1}^{|C|} \mathbf{x}_{ki} w_i^{-1}}{\sum_{i=1}^{|C|} w_i^{-1}} \tag{5.16}$$

.

$$\mathbf{P}_k = \frac{\sum_{i=1}^{|C|} \mathbf{P}_{ki} w_i^{-1}}{\sum_{i=1}^{|C|} w_i^{-1}} \tag{5.17}$$

.

6 Simulations and Experiments

In this chapter, simulations and real world-experiments are demonstrated and the results are discussed.

6.1 Simulations

6.1.1 Simulation Setup

These experiments are all simulated in MATLAB. The simulated scenario has the size of 150m by 150m. The trajectory of the mobile tag is generated with the random walk model. In this model, the initial state $\mathbf{x}_0$ is shown as Equation 6.1. Since the average walking speed of human is 5 kilometres per hour [31], i.e, 1.4 meters per second, so we chose this value for the initial velocity $\dot{p}$. With the relation as shown in Equation 6.2, we choose $1m/s$ as the value for $\dot{p}_x$ and $\dot{p}_y$.

$$\mathbf{x}_0 = \begin{bmatrix} p_x \\ p_y \\ \dot{p}_x \\ \dot{p}_y \end{bmatrix} = \begin{bmatrix} 0 \\ 0 \\ 1 \\ 1 \end{bmatrix} \tag{6.1}$$

.

$$\dot{p}^2 = \dot{p}_x^2 + \dot{p}_y^2 \tag{6.2}$$

And the accelerations $\ddot{p}_x$, $\ddot{p}_y$ are randomly changing value, which will change for each point in the trajectory, thus changes the state vector. The time intervals between each two consecutive points are always 0.5 second, which are close to the sampling rate of the UWB measurement system in a real world experiment. The generated trajectory is shown in Figure 6.1.

4 anchor nodes are placed at the corner of this scenario, as shown as red diamonds in Figure 6.1. When choosing the positions of the nodes, it should be noticed that the nodes should be away from most of the tag's points for at least 2 meters. Besides, it is also good when at least 3 nodes are 2 meters away from every tag's point. This is because of the 2-meters-error-range problem as mentioned in section 4.2.

Based on the known positions of the nodes and tag's trajectory, the true distances between every node i and every tag's points j can be determined. These true distances corrupted with noises r_i leads to the simulated measurements data d_{ij}. The noise r_i follows $\mathbf{r}_i \sim \mathcal{N}(0, \sigma_i^2)$, where σ_i is determined according to Table 4.4.
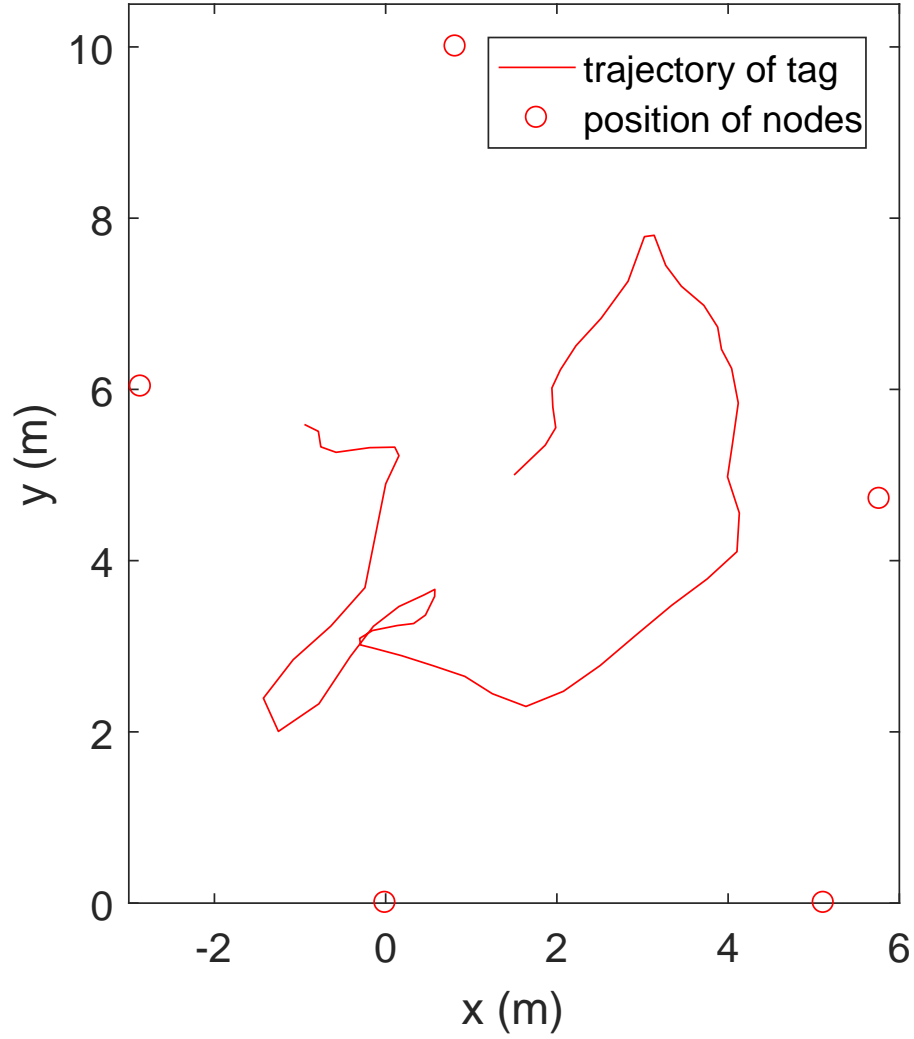
Figure 6.1: Trajectory generated with random walk model. Positions of nodes are marked with red diamonds

Besides, part of the simulated measurements data are randomly chosen and deleted to simulate the case, where measurements data are not obtained.

With the positions of the anchor nodes and the simulated measurements data, we proceed the experiment with the above mentioned algorithms.

6.1.2 Results

With the well tuned parameters, the estimates of position by three algorithms (EKF-MC1, EKF-MC2, and OM) are shown in Figure 6.2. And the estimates of velocities of the tag are plotted in Figure 6.3.
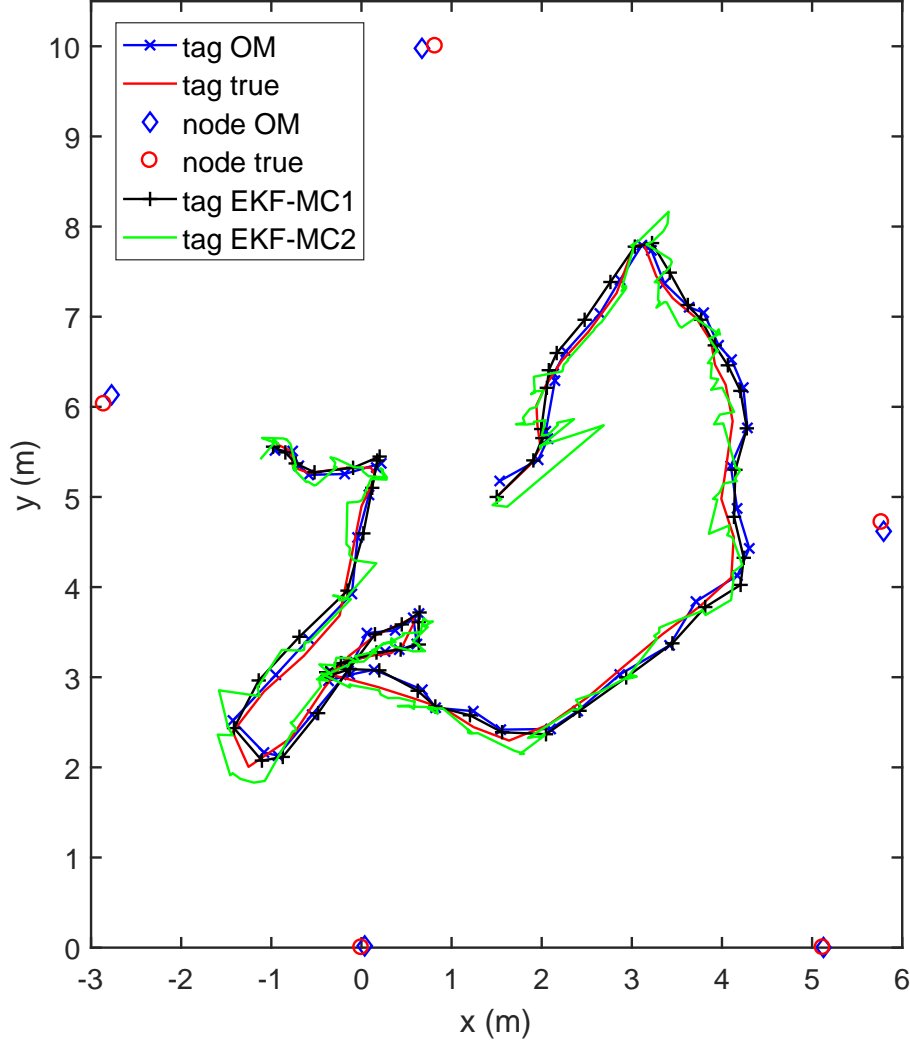
Figure 6.2: Estimates of position v.s. ground true positions (in simulation)

The performance of the algorithms is judged by the mismatches of the estimated positions and velocities to the true ones. These mismatches are considered as errors. The errors are judged by Root-Mean-Square Error (RMSE), maximum and minimum absolute error. The RMSE of estimation for positions and velocities are calculated as in Equation 6.3 and Equation 6.4,

$$\text{RMSE}_\text{p} = \sqrt{\frac{\sum_{i=0}^{n} \|\hat{\mathbf{p}}_i - \mathbf{p}_i\|^2}{n}}, \tag{6.3}$$

$$\text{RMSE}_{\dot{\text{p}}} = \sqrt{\frac{\sum_{i=0}^{n} \left\|\hat{\dot{\mathbf{p}}}_i - \dot{\mathbf{p}}_i\right\|^2}{n}}, \tag{6.4}$$
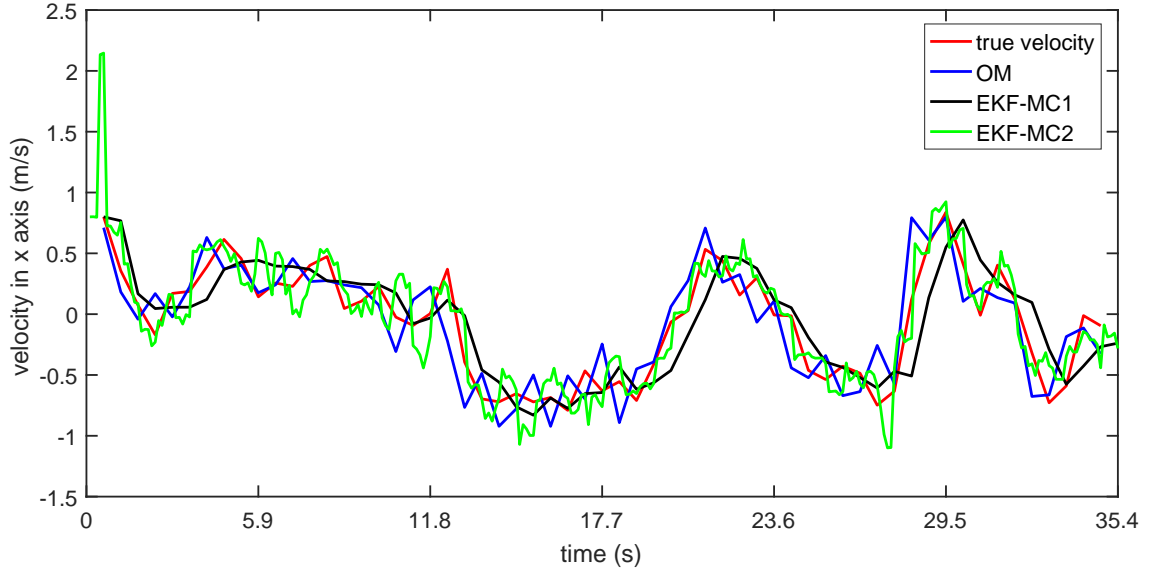
(a)
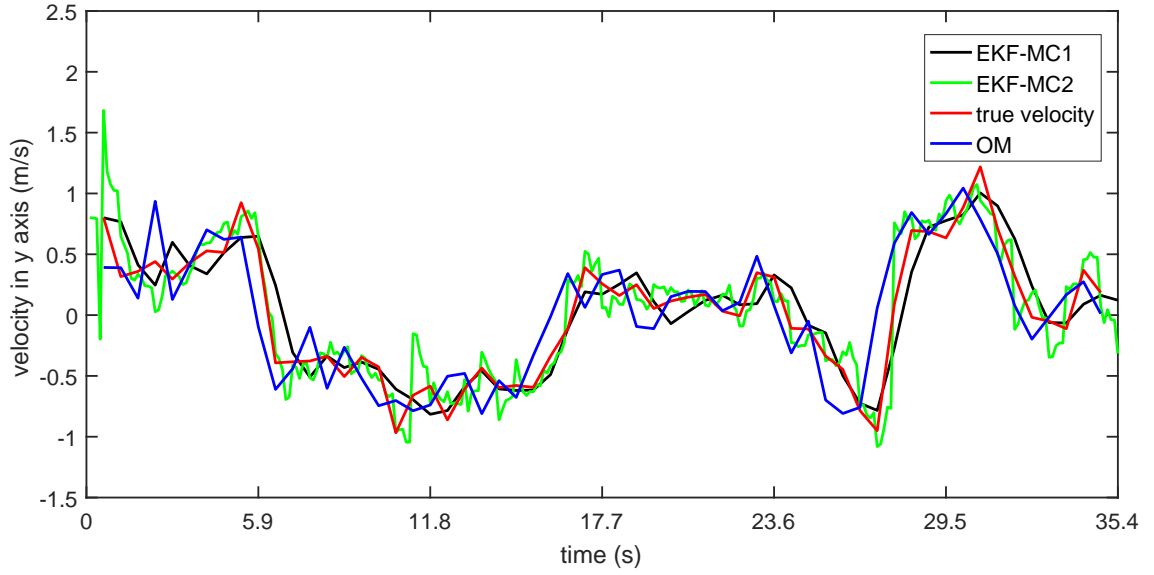
(b)

Figure 6.3: Estimates of velocities v.s. true velocities, (a)velocity in x axis, (b)velocity in y axis

where n is the total number of points in the trajectory, $\hat{\mathbf{p}}_\mathbf{i}$ and $\dot{\hat{\mathbf{p}}}_i$ are the estimate positions and velocities from the algorithm, while $\mathbf{p}_i$ and $\dot{\mathbf{p}}_i$ the true ones, $\|\cdot\|$ calculates the Euclidean distance.

Table 6.1 and Table 6.2 list the values of these errors. The EKF-MC1 has the smallest RMSE and minimum absolute error in both velocity and position. It also has the smallest minimum absolute error in position and the second smallest minimum absolute error in velocity, which is still very close to the smallest one 0. However The EKF-MC2 has largest maximum absolute error in both velocity and

44

position, also the largest RMSE in velocity. Overall, the EKF-MC1 performs best, while the EKF-MC2 performs worst. This could be caused by the fact that the parameters of the transition model in EKF are not optimal tuned. Since the EKF-MC2 updates once with only one measurement data, it depends heavily on a good transition model.

Table 6.1: Errors in estimates of position by different algorithms in simulation.

Errors (m) Algorithms	RMSE	| Min |	| Max |
EKF-MC1	0.1475	0.0010	0.3236
EKF-MC2	0.1523	0.0010	0.9487
OM	0.1565	0.0180	0.3419

Table 6.2: Errors in estimates of velocities by different algorithms in simulation.

Errors (m/s) Algorithms	RMSE	| Min |	| Max |
EKF-MC1	0.2188	0.0073	0.7167
EKF-MC2	0.4196	0.0001	2.2369
OM	0.3778	0.0380	1.1214

Figure 6.4 shows the histograms of the estimation errors of EKF-MC1 with respect to position and velocity. The data comes from a similar simulation that contained 600 measurement sets. In the same figures, distribution density functions, which best fit to the histogram, are also plotted. Subplots (a), (b), (c) and (d) are about the errors of position and velocity in x- and y-axis. They have the similar shape of Gaussian distribution. Subplots (e) and (f) are about the absolute errors of position and velocity. They have the similar shape of Rayleigh distribution. This can be explained by the fact that, these absolute errors can be interpreted as the square root of the sum of square of errors in x- and y-axis. If the errors in x- and y-axis followed Gaussian distributions, the correspond absolute error should follow a Rayleigh distribution. However, when the normality tests [32], such as *Lilliefors test*, *Jarque-Bera test*, *Chi-square goodness-of-fit test* and *One-sample Kolmogorov-Smirnov test* are applied to data to test for the null hypothesis that the errors in x- and y-axis come from a normal distribution, rejections at the 5% significance level are obtained for most cases. For this reason, we could not draw the conclusion that they follow Gaussian distribution. Table 6.3 shows this test results.

Figure 6.5 and Figure 6.6 shows the histograms of the estimation errors of EKF-MC2 and OM with respect to position and velocity. Again, no conclusion can be drawn that they follow Gaussian distribution.
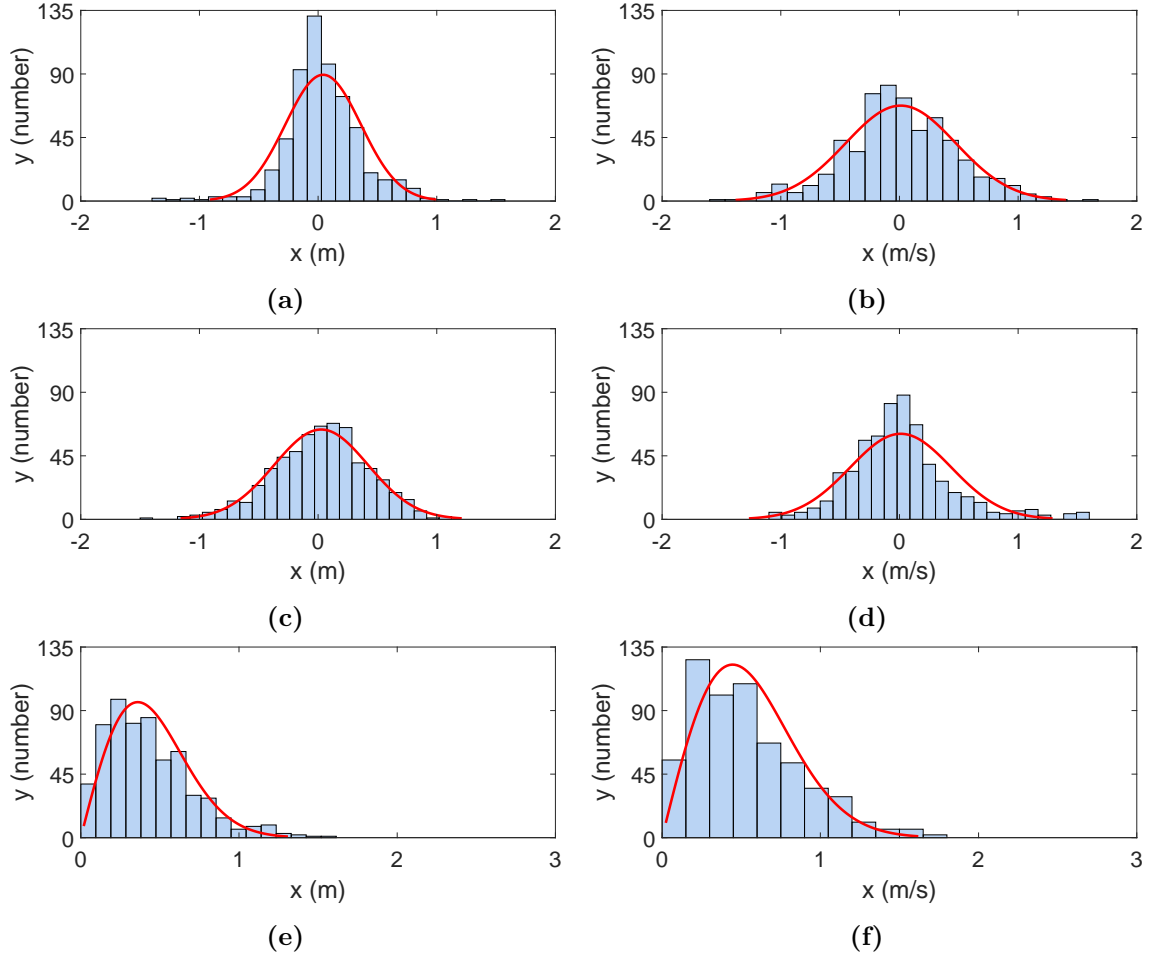
Figure 6.4: Histogram of estimation errors by EKF-MC1. (a)(c)(e) are position errors in x-axis, in y-axis, and absolute error. (b)(d)(f) are velocities errors.

Table 6.3: Normality tests results for errors, 1 for rejection at the 5% significance level, 0 otherwise.

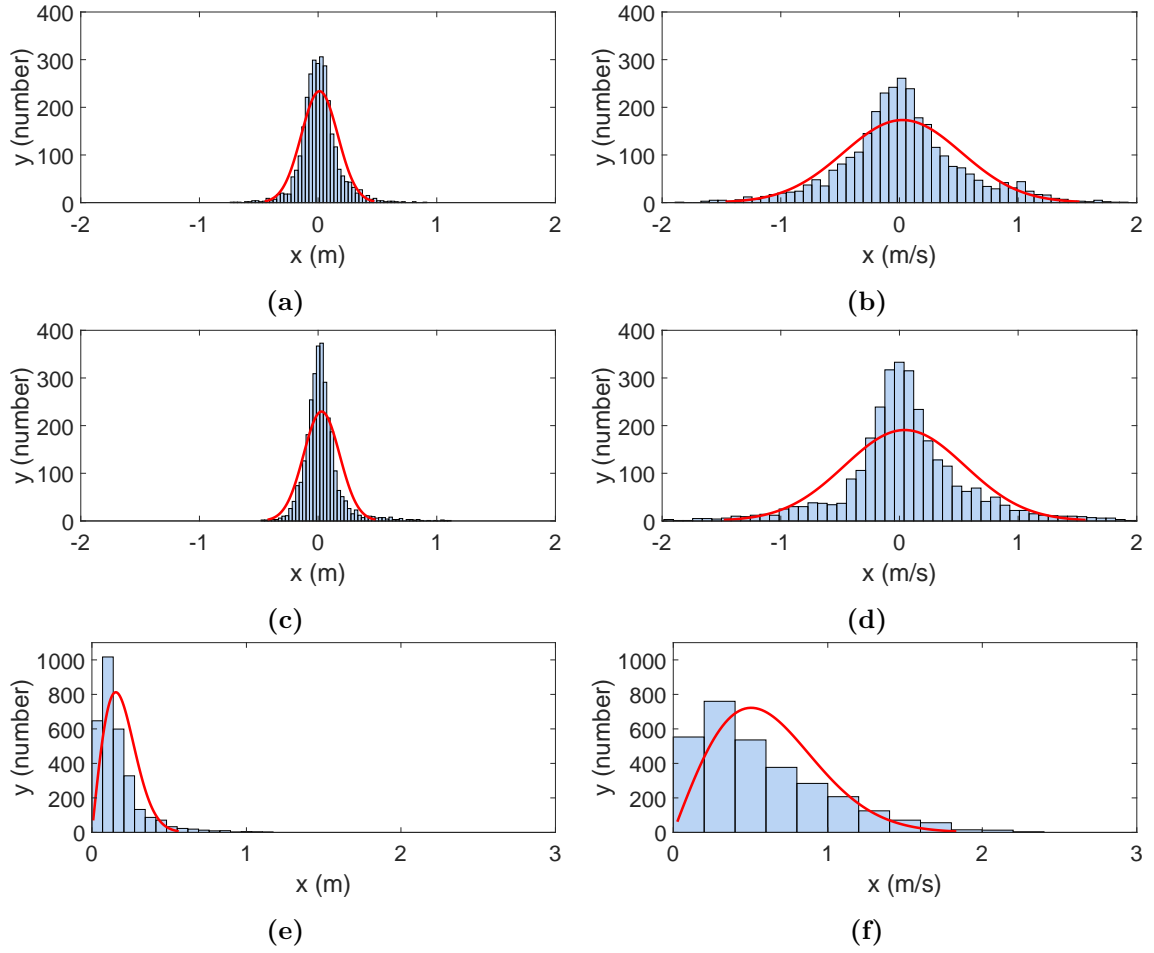|	Errors Tests	position(x)	position(y)	velocity(x)	velocity(y)
EKF-MC1	Lilliefors	1	0	1	1
	Jarque-Bera	1	1	0	1
	Kolmogorov-S	1	1	1	1
	Chi-square	1	0	1	1
EKF-MC2	Lilliefors	1	1	1	1
	Jarque-Bera	1	0	1	1
	Kolmogorov-S	1	1	1	1
	Chi-square	1	1	1	1
OM	Lilliefors	1	1	1	1
	Jarque-Bera	1	0	1	1
	Kolmogorov-S	1	1	1	1
	Chi-square	1	1	1	1

Figure 6.5: Histogram of estimation errors by EKF-MC2. (a)(c)(e) are position errors in x-axis, in y-axis, and absolute error. (b)(d)(f) are velocities errors.
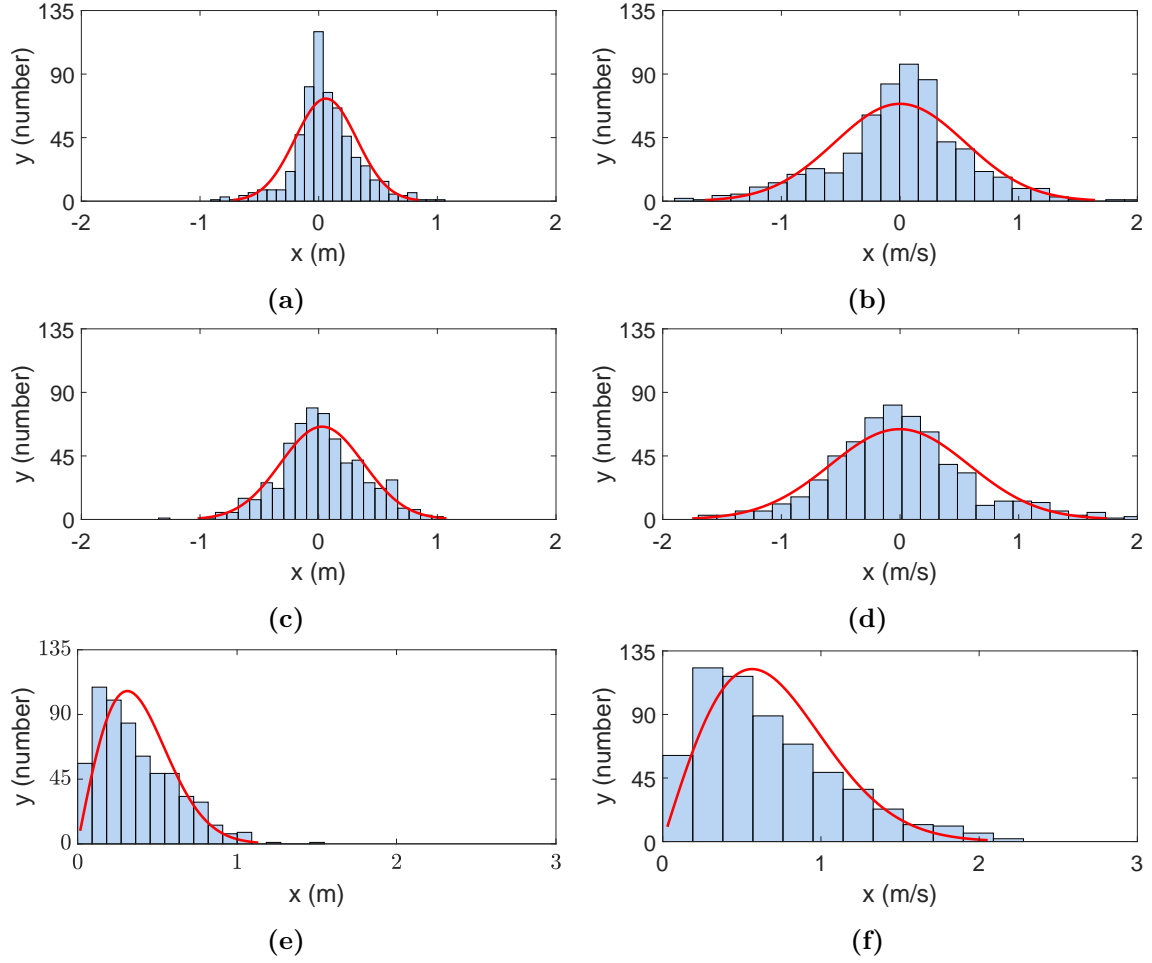
Figure 6.6: Histogram of estimation errors by OM algorithm. (a)(c)(e) are position errors in x-axis, in y-axis, and absolute error. (b)(d)(f) are velocities errors.

6.2 Experiments based on Measurement Data

6.2.1 Experiment Setup

The real world experiments are done in a empty hall of building 78 in Faculty of Engineering, University Freiburg. 5 anchor nodes were placed inside the hall and 1 mobile tag was moving in trajectories with the shape of squares and circles. Figure 6.7 is a picture of the experiment environment. The base station and anchor nodes were placed on top of pillars, $30cm$ above from the ground to reduce the signal the affect from reflections from the ground. The tag was attached to a stick with the same $30cm$ above from the ground. On the top of the moving stick is a marker, which passively reflect the signal from the motion capture (Mo-cap) system and served as the target of this Mo-cap system. The Mo-cap system has the resolution of millimeters, which is much higher then our UWB system. For this reason, the trajectory of the marker recovered by the Mo-cap system can be served as the ground true of the tag's trajectory for further comparison.
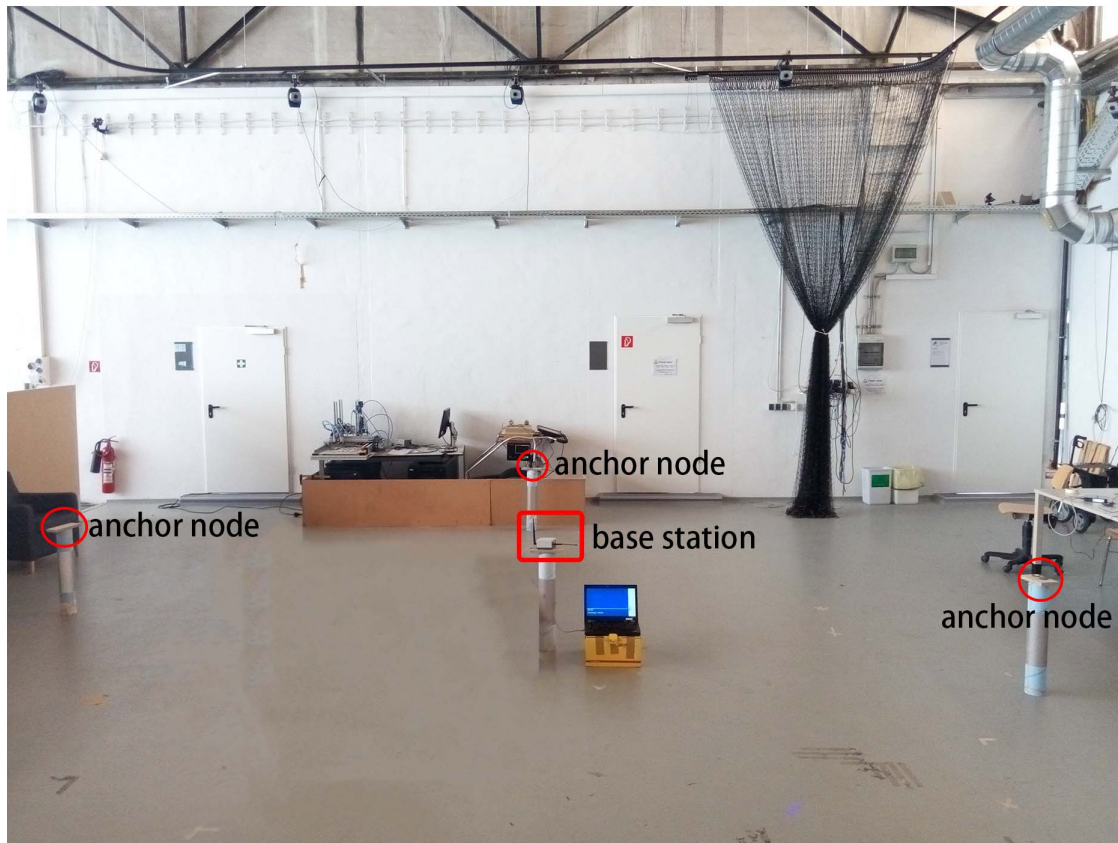

Figure 6.7: Experiment environment.

6.2.2 Results

Using the obtained measurements data in a experiment where the tag was moved in a square form trajectory, the estimates of trajectory from EKF-MC1, EKF-MC2 and OM are plotted in Figure 6.8. Since the EKF-LWCR is developed based on EKF-MC1 for errors mitigation purpose, its performance is mainly evaluated by comparing its estimates of trajectory to the ones by EKF-MC1. These two estimates together with the true trajectory are plotted in Figure 6.9.
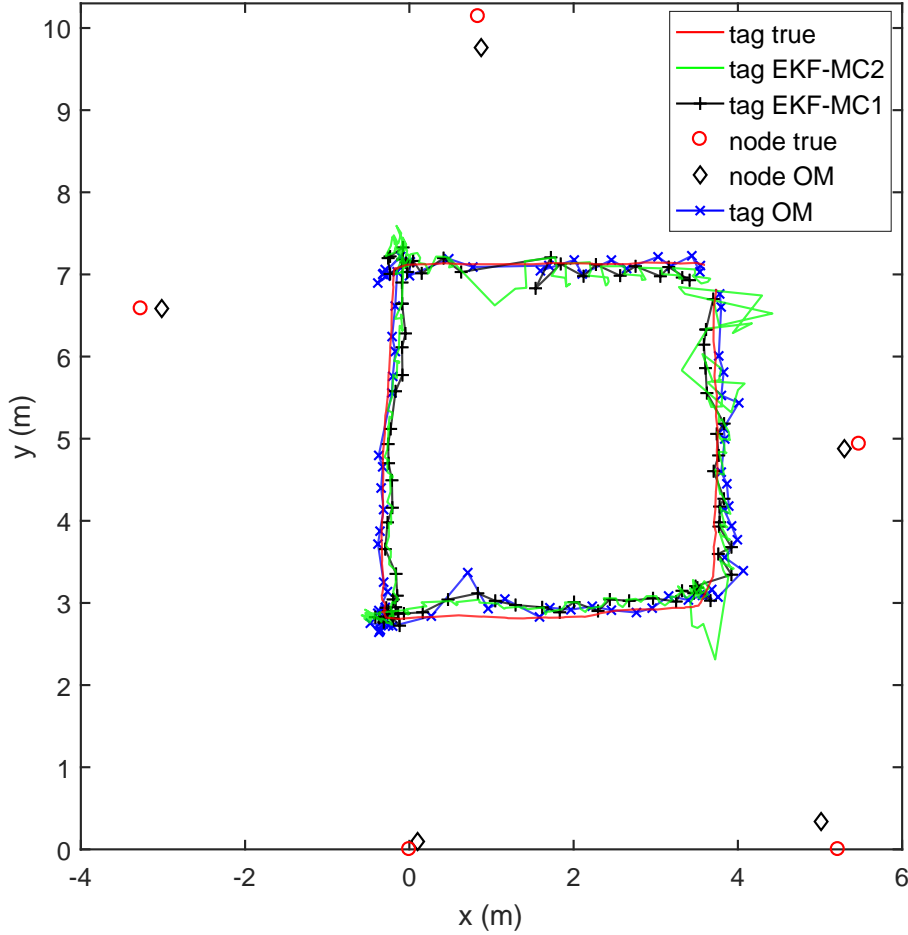
Figure 6.8: Estimates of position by EKF-MC1, EKF-MC2 and OM v.s. ground true positions (square trajectory)

In Figure 6.8, it is worth noting that the estimated trajectory of the EKF-MC2 has large errors at the beginning, this could be caused by a bad initial guess for the state vector $\mathbf{x}_0$ or a bad initial guess for the error covariance matrix $\mathbf{P}_0$. Since EKF-MC2 updates each time with only one measurement data, the state stabilizes very slowly. Besides, large errors also happens at the corners, especially at the upper-left and the bottom-right corners. These might be caused by the value for $\mathbf{Q}$ are chosen too small so that the EKF has weighted the prediction steps more than it should have.
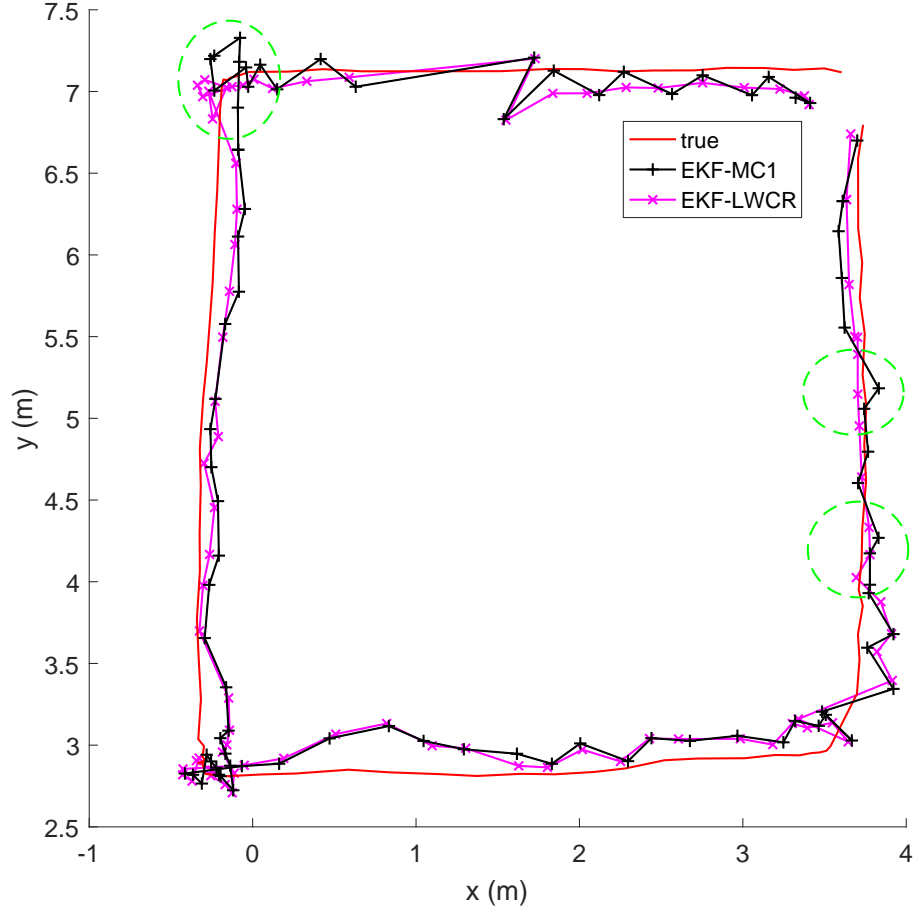
Figure 6.9: Estimates of position by EKF-LWCR and EKF-MC1 v.s. ground true positions (square trajectory)

It is noteworthy that the errors of estimates of positions of the anchor nodes by the OM are distinct. The errors are listed in Table 6.4. It is also worth noting that, compared to the true positions of the nodes, the estimated positions are all closer to the center, where the base station is located. This could be cause by the non-linear relation between the measured value and the true one when distances are less than two meters, in which cases the measured value would be smaller as the true one [12]. As can be seen in Figure 6.8, distances between part of the right side of the trajectory and the rightest anchor node is less than two meters. With this 'shorten' measurements, the optimization could have the estimation of the position of the nodes closer to the trajectory.

Table 6.4: Errors in estimates of position of nodes by OM algorithm

	node 1	node 2	node 3	node 4	node 5
Errors (m)	0.1802	0.3978	0.1413	0.2511	0.3489

52

As can be seen in Figure 6.9, most of the positions estimates from EKF-MC1 and EKF-LWCR are nearly the same, except for some positions marked with green ellipsoids in dash line. On the one hand, within these green ellipsoids, the estimates of the EKF-LWCR have shorter Euclidean distance to the true ones than the ones by EKF-MC1. This can be an indication that the EKF-LWCR can mitigate the measurement errors well and reduce the estimates errors caused by NLOS. On the other hand, the fact that the estimates of the two algorithms are very close for most of the time indicates that the UWB ranging system have a robust performance against NLOS error.

The position estimates errors from the four algorithms are list in Table 6.5. Within the three algorithms without NLOS errors mitigation (EKF-MC1, EKF-MC2 and OM), the OM has the smallest RMSE $0.2126\,m$ and the smallest minimum absolute error $0.0041\,m$, while the EKF-MC2 has the largest RMSE $0.2454\,m$ and the largest maximum absolute error $0.9167\,m$. Meanwhile the EKF-MC1 has the smallest maximum absolute error $0.4131\,m$. These results might caused by the outliers in the measurements data, i.e. the measurements with great noises or errors. The EKF-MC2 updated once with only one distance measurement data. The OM optimized the position of point with a whole measurements set (containing 3 to 5 measurements), however, the correlation between the consecutive points are not considered. With these reasons, these two algorithms are relatively sensitive to the outliers in the measurements data. In contract, the EKF-MC1 updated once with a whole set of data and considered the correlation between the consecutive points in the prediction step, this makes it relatively robust with the existence of outliers. On the other hand, the EKF-LWCR has the smallest RMSE among the four algorithms, which could be served as a proof that the EKF-LWCR can successfully mitigate the outliers (measurements containing NLOS error).

Table 6.5: Errors in estimates of position by different algorithms

Errors (m) Algorithms	RMSE	| Min |	| Max |
EKF-LWCR	0.1987	0.0071	0.42352
EKF-MC1	0.2188	0.0073	0.4131
EKF-MC2	0.2454	0.0090	0.9167
OM	0.2126	0.0041	0.6312

The estimates of velocities in x- and y-axis from EKF-MC1, EKF-MC2 and OM are plotted in Figure 6.10. As mentioned above, to observe the performance of EKF-LWCR against NLOS errors, the estimates of velocities from EKF-LWCR are compared only to ones from EKF-MC1. Figure 6.11 plots the estimates errors of these two algorithms. And Table 6.6 lists the velocity estimated errors of these four algorithms.

As can be seen in Figure 6.10, the estimates of velocities by EKF-MC2 has large errors at the beginning, resulting in the largest maximum absolute error among
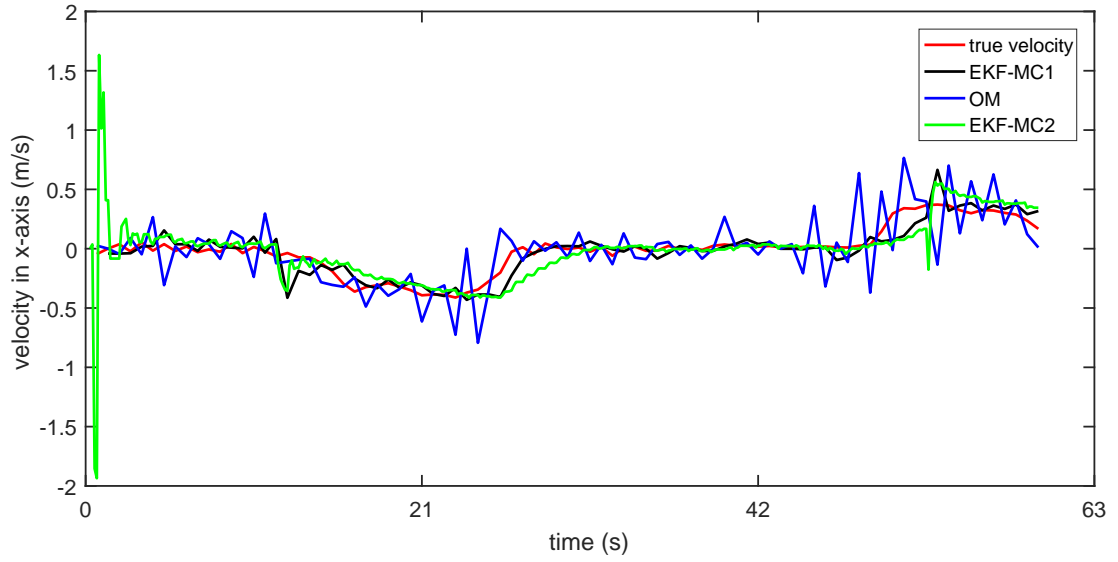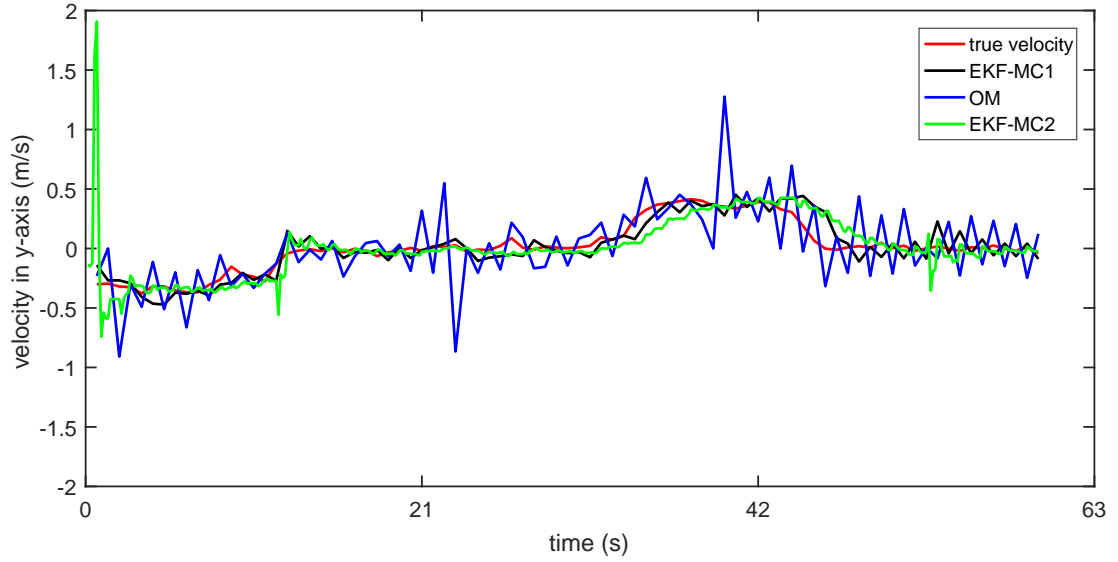
Figure 6.10: Estimates of velocities by EKF-MC1, EKF-MC2, and OM and v.s. true velocities (square trajectory). (a)velocity in x-axis, (b)velocity in y-axis

Table 6.6: Errors in estimates of velocities by different algorithms

Errors (m/s) Algorithms	RMSE	| Min |	| Max |
EKF-LWCR	0.1326	0.0136	0.4593
EKF-MC1	0.1333	0.0105	0.4220
EKF-MC2	0.2715	0.0068	2.8964
OM	0.3685	0.0287	1.0298

54

(a)

(b)
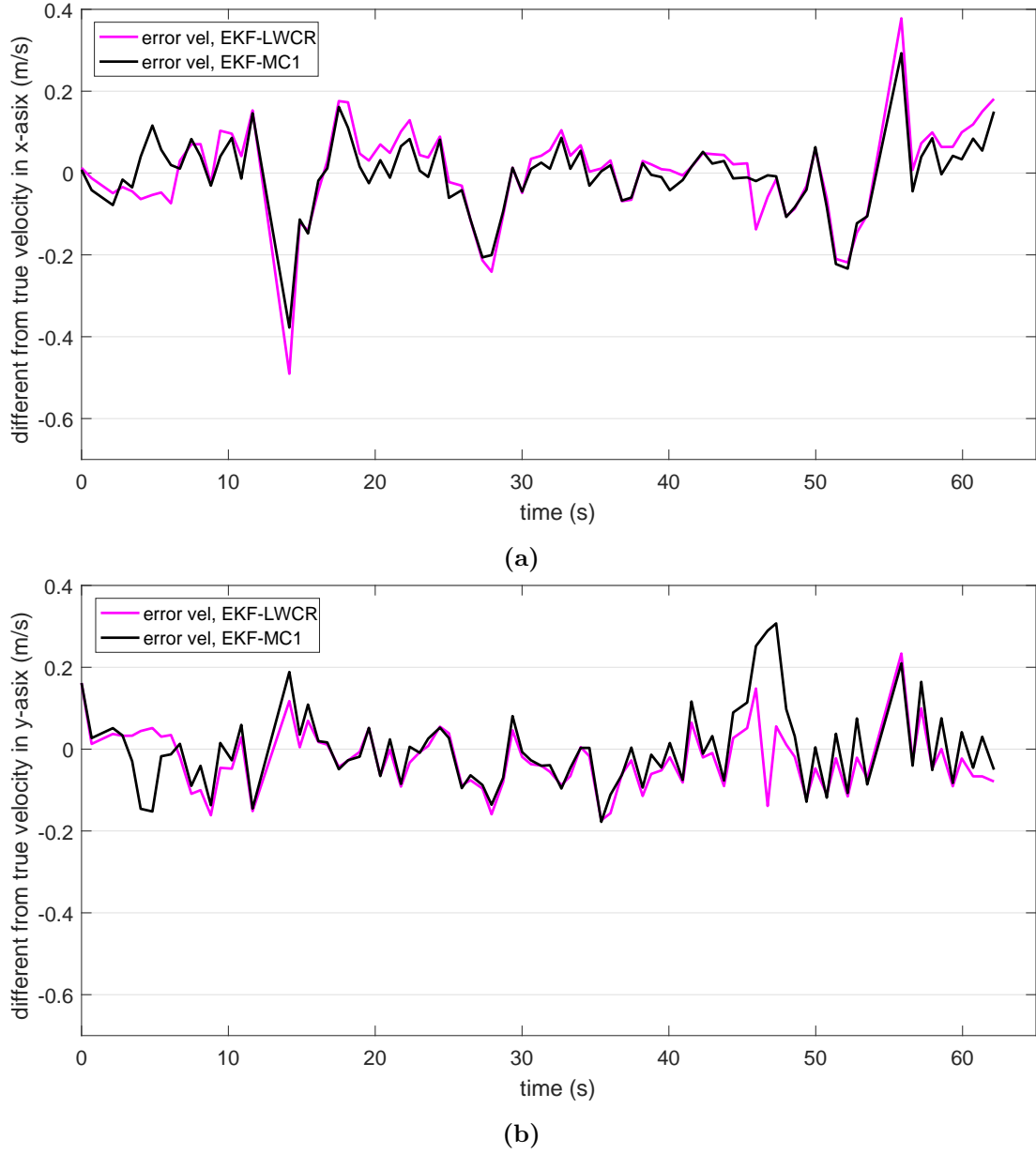
Figure 6.11: Errors in estimates of velocities by EKF-MC1 and EKF-LWCR (square-shape tra-
jectory). (a)errors in x-axis, (b)errors in y-axis

these algorithms with the value of $2.8964\ m/s$, as shown in Table 6.6. This could be
caused by the same reason as mentioned above: slow convergence to the true value.
Another reason could be a bad initial guess for $\mathbf{x}_0$ and $\mathbf{P}_0$. Meanwhile, the estimates
of velocities by the OM have greater oscillations than others, resulting in the largest
RMSE value among these algorithms with the value of $0.3685\ m/s$. This might be
caused by the absence of the correlations between each two adjacent points.

According to Figure 6.11, the estimates errors of the EKF-LWCR are sometimes
larger than the ones by the EKF-MC1, while sometimes smaller. Overall, it can

not concluded which one performs better than the other. Table 6.6 shows that the EKF-LWCR has a smaller RMSE than the EKF-MC1, but the difference is too small to convince the EKF-LWCR has better estimates of velocities than the EKF-MC1.

Figure 6.12 shows the histograms of the estimate errors of EKF-MC2 with respect to position and velocity. The Gaussian and Rayleigh distribution density functions, which best fit to the histogram, are also plotted. Different to as discussed in subsection 6.1.2, most of these histograms do not have good shapes of Gaussian or Rayleigh distributions, this could be cause by the fact that the number of data is too small to recover these expected distributions, or that the errors are not following these distributions. And the same normality tests as in subsection 6.1.2, reject the hypothesis that the errors come from a normal distribution at the 5% significance level.

The same results have been obtained for the analysis of the distributions of estimate errors by EKF-MC1, EKF-LWCR and OM. Limited to the length of this article, these histograms of them are not shown here.
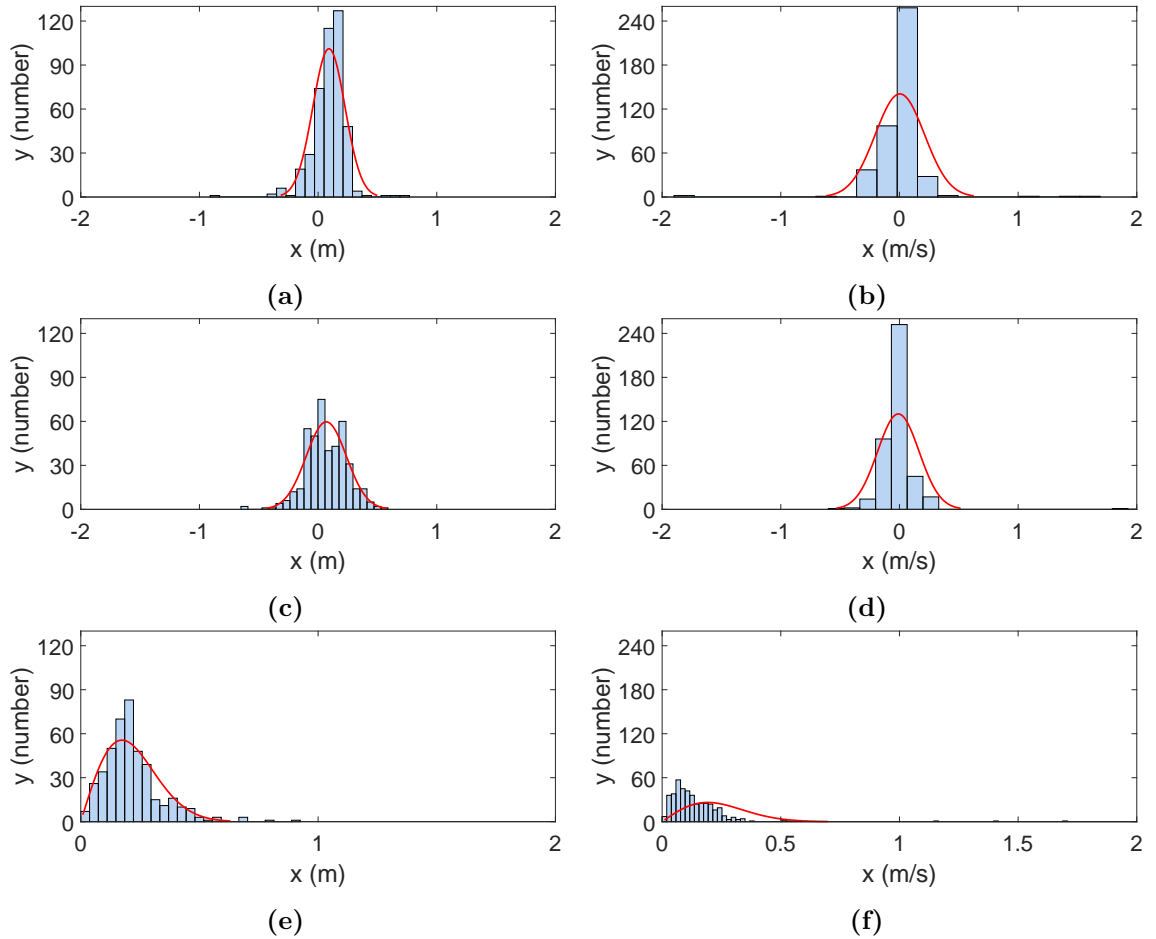

Figure 6.12: Histogram of estimation errors by EKF-MC2 based on measurement data. (a)(c)(e) are position errors in x-axis, in y-axis, and absolute error. (b)(d)(f) are velocities errors.

Another experiment is done with the same setup, in which, however, the tag was moved around a circle. Using the obtained measurements data, the estimated trajectories from the 3 algorithms without error mitigation (EKF-MC1, EKF-MC2 and OM) are plotted in Figure 6.13, while the comparison of estimates of positions between EKF-LWCR and EKF-MC1 are shown in Figure 6.14.
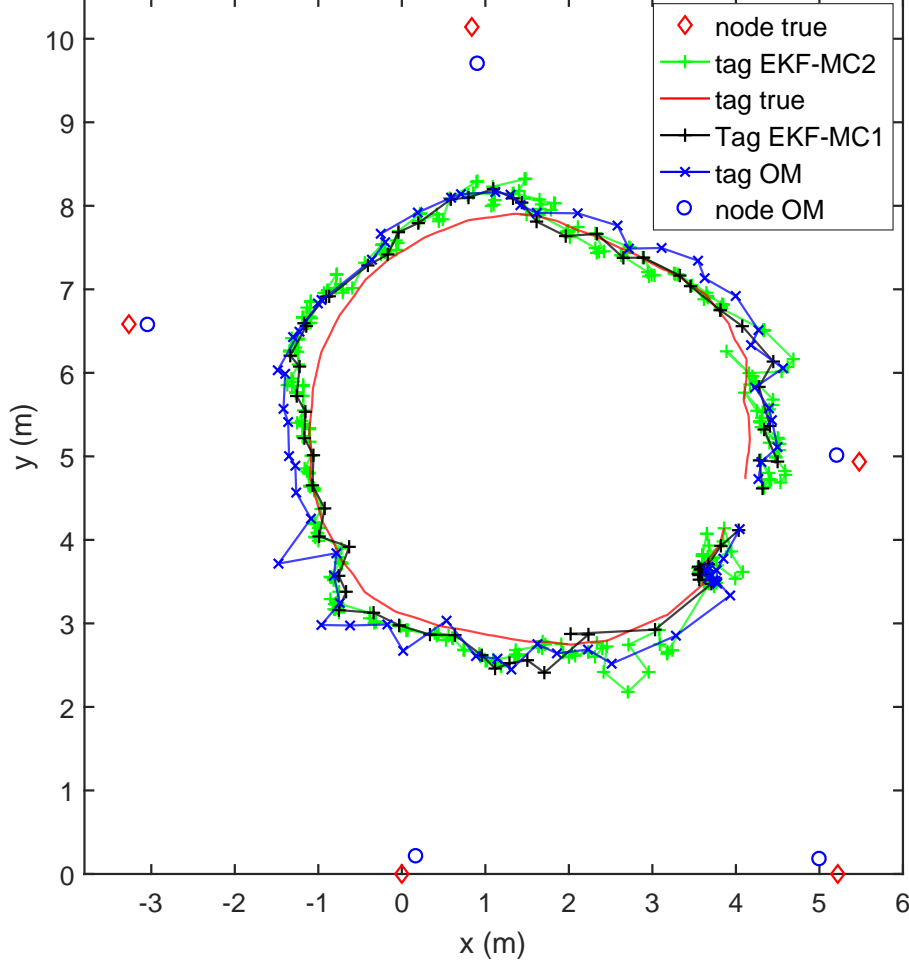
Figure 6.13: Estimates of position by EKF-MC1, EKF-MC2 and OM v.s. ground true positions (circle trajectory).

When comparing Figure 6.13 to Figure 6.8, it is noteworthy that the estimated trajectory of the EKF-MC2 does not have large errors at the beginning, which could be the result of a better initial guess of $\mathbf{x}_0$ and $\mathbf{P}_0$ than the one in Figure 6.8. It is also noteworthy that the nodes positions of the anchor nodes estimated by the OM are almost the same for both 2 experiments.

In Figure 6.14, the estimates with conspicuous difference are marked with green ellipses in dash line. Within these green ellipses, compared with the EKF-MC1's estimates, the estimates from EKF-LWCR obviously have shorter Euclidean distances to the true ones. This again could be served as a proof that the EKF-LWCR can successfully reduce the estimates errors caused by outliers (measurements containing
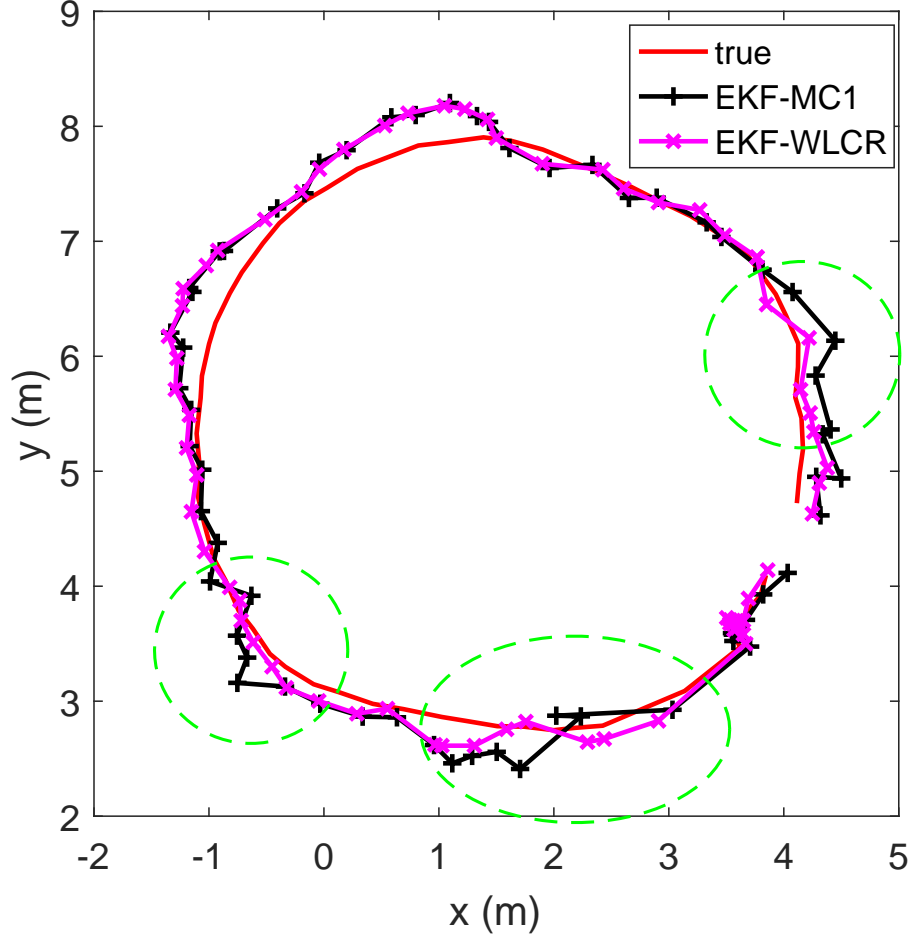
Figure 6.14: Estimates of position by EKF-LWCR and EKF-MC1 v.s. ground true positions (circle trajectory).

NLOS error). On the other hand, most of the estimates of the two algorithms are very similar, indicating that the UWB ranging system have a robust performance against NLOS errors.

The errors of the estimates of trajectory by these four algorithms are list in Table 6.7. The EKF-LWCR has the smallest RMSE and maximum absolute error among the four algorithms, which again indicates the EKF-LWCR can reduce the estimates errors caused by outliers.

The estimates of the velocity by EKF-MC1, EKF-MC2 and OM are plotted in Figure 6.15. It is worth noting that in Figure 6.15, the velocities of the mobile tag estimated by EKF-MC1 have sharp jumps from the 10th s to the 15th s, this might be estimated error due to the fact that the time intervals between two adjacent estimations are too large. Between this 5 s time gap, there are only 4 estimates. The time intervals between each these estimates are 1.25 s, while the rest have the average value of 0.7 s. This might be caused by measurements data missing. However, the estimates of velocities afterwards are still able to converge close to the

Table 6.7: Errors in estimates of position by different algorithms (circle trajectory)

Errors (m) Algorithms	RMSE	| Min |	| Max |
EKF-LWCR	0.2523	0.0190	0.4215
EKF-MC1	0.2842	0.0161	0.4470
EKF-MC2	0.2727	0.0620	0.4365
OM	0.2950	0.0116	0.6731

true value. It is also worth noting that, the estimates by OM has the same large oscillation as the one in Figure 6.10, which might be caused by the absence of the correlations between each two adjacent points.

Figure 6.16 plots the estimates errors of velocities by the EKF-MC1 and the EKF-LWCR. It can be observed that the estimates errors are both very large when the time intervals for EKF updates are large, but the oscillation of the errors by the EKF-LWCR is more gentle.

Table 6.8 lists the velocity estimated errors of these four algorithms. Unlike the results from last experiment, in this experiments, due to the absence of measurements for long time (1.25 s), the EKF-LWCR and EKF-MC1 have the largest RMSE and maximum absolute error among the four algorithms.

When analyze the distributions of estimate errors by the four algorithms in this experiment. The similar results as the ones from experiment by square-shape trajectory have been obtained. Most of the histograms of errors in this experiment do not have good shapes of Gaussian or Rayleigh distributions, the reason of which could be that the number of data is too small to recover these expected distributions, or the errors are not following these distributions. The normality tests in subsection 6.1.2 also reject the hypothesis that the errors come from a normal distribution at the 5% significance level. Limited to the length of this article, these histograms of the errors are not shown here.

Table 6.8: Errors in estimates of velocities by different algorithms (circle trajectory)

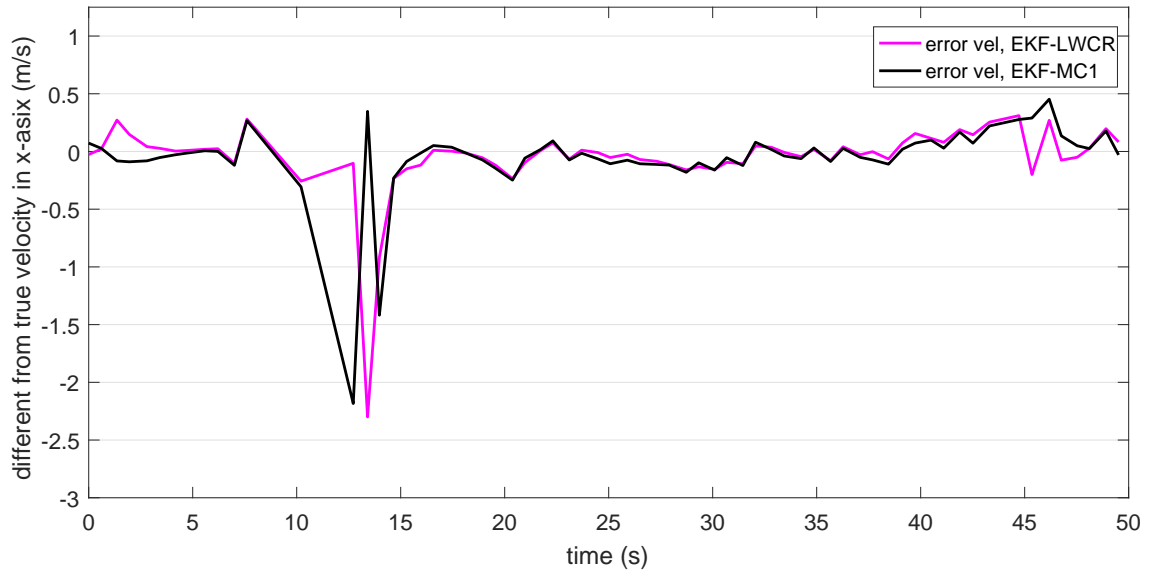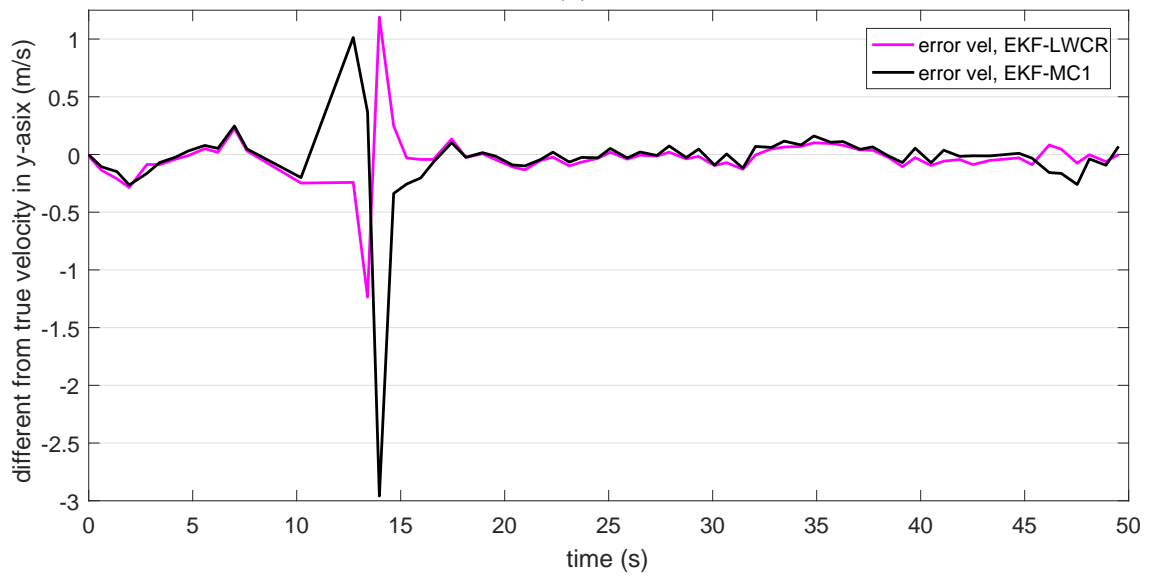| Errors (m/s) Algorithms	RMSE	| Min |	| Max |
EKF-LWCR	1.9636	0.0176	2.5830
EKF-MC1	2.0218	0.0128	3.572
EKF-MC2	0.1323	0.0027	1.143
OM	0.3162	0.0135	1.216
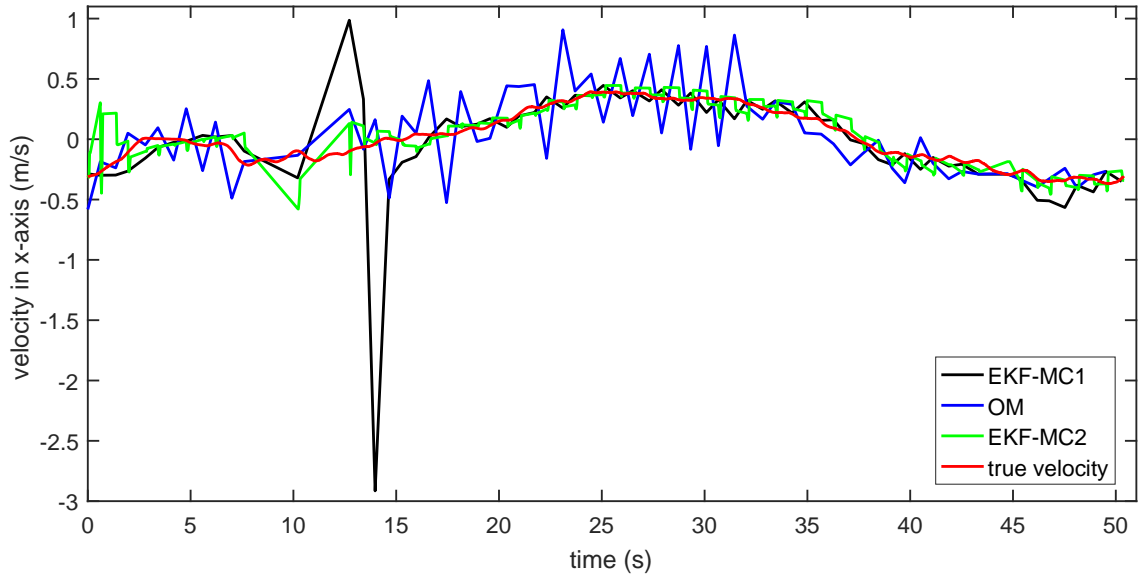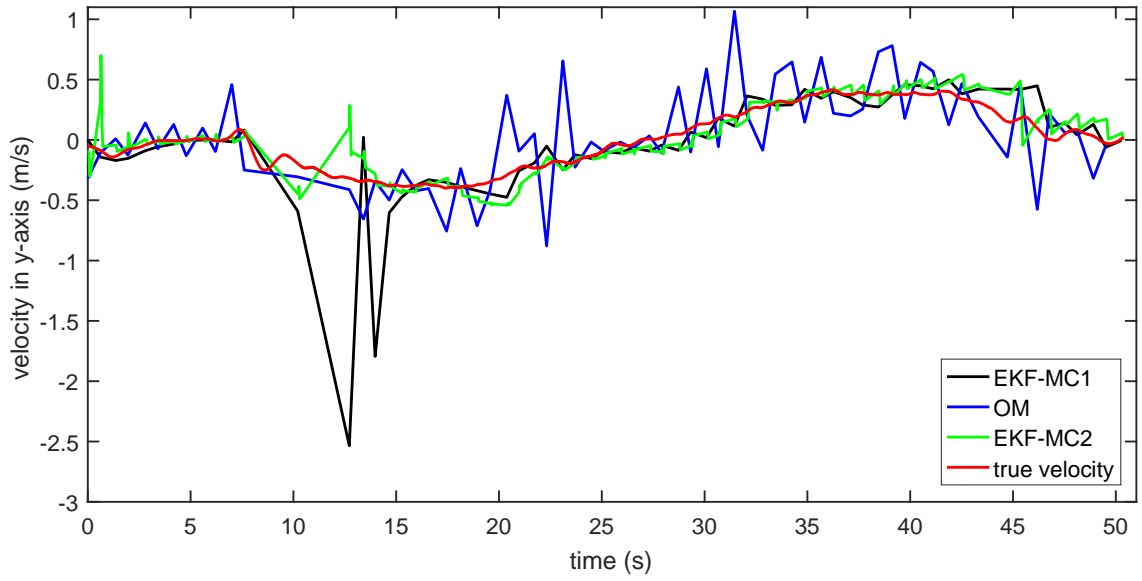
Figure 6.15: Estimates of velocities by EKF-MC1, EKF-MC2, and OM v.s. true velocities (circle trajectory). (a)velocity in x-axis, (b)velocity in y-axis

Figure 6.16: Errors in estimates of velocities by EKF-MC1 and EKF-LWCR (circle trajectory). (a)velocity in x-axis, (b)velocity in y-axis

7 Summary and Outlook

7.1 Summary of the Work

In this master thesis, we presented a novel UWB ranging system for indoor localization.

The ranging procedure of this system based on the principle of double sided two way ranging has been presented. The reasons for the poor performance of the original ranging system have been explained and analyzed. And significant improvements in the performance of the ranging system has been achieved, by adding a mutual exclusion mechanism to prevent the system from useless looping, together with changing system setting, such as sleeping mode, timing in real time counters and loop end conditions. The sampling rate of the ranging system has been improved from 0.2 Hz to 1.5 Hz, increased by seven times. The total measurement obtained rate has doubled from 0.46 to 0.84. Besides, the occurrence rate of the measurements sets which contain more than two valid measurements has been increased from 0.4 to 0.9. With these enhanced performances, the ranging system is capable of localizing a moving target with a human walking speed in high resolution.

The calibrations for the ranging system have also been done. The calibration parameters have been determined by applying linear regression to the data collected by different anchor nodes with different distances. Meanwhile, the variances of the measurements of different anchor nodes have also been calculated, which are used to determine the observation noise matrices of the EKF. Besides, the distributions of the measurements data with certain distances have been analyzed. Although these distributions have the shapes similar to normal distributions, there is no enough evidence from normality tests can prove that the data are normally distributed.

Four different algorithms for localization, which are the EKF-MC1, the EKF-MC2, the EKF-LWCR, and the OM, have been built and tested with both simulated data and data collected by the UWB ranging system in real-world experiments. In the simulation, the trajectory of the target was generated by random walk model while in the experiments, the target was moving around a circle and a square. All these four algorithms can recover the trajectories of the moving target, but with different accuracy. Their RMSE varies from 0.20 m to 0.24 m in position estimation and from 0.13 m/s to 0.37 m/s in velocity estimation for different algorithms. The four algorithms have different advantages and disadvantages. The EKF-LWCR can reduce the errors in estimates of position caused by measurement outliers without identifying them. However, the EKF-LWCR has relative large errors in estimates of velocity when the time intervals between estimates are larger than 1 s. The

EKF-MC1 has slightly larger errors in estimates of position than the EKF-LWCR, but its computational consumption is smaller than the one of the EKF-LWCR. However, like the EKF-LWCR, the EKF-MC1 also gets large errors in estimates of velocity when the time intervals between estimates are large. The EKF-MC2 is more sensitive to bad initial guesses of states, but it has better estimates of velocity than the EKF-LWCR and the EKF-MC1 when the time intervals between estimates are large. The OM can estimate the positions of nodes and tag simultaneously. However, in comparison with the other algorithms, its estimates of velocity have larger oscillation around the true value. Furthermore, the distributions of the errors in estimates have been analyzed, still, there is no enough evidence from normality tests can prove that the errors are normally distributed.

A comparison about the accuracy of position estimation between this UWB localization system and other system based on different technologies is illustrated in Figure 7.1.
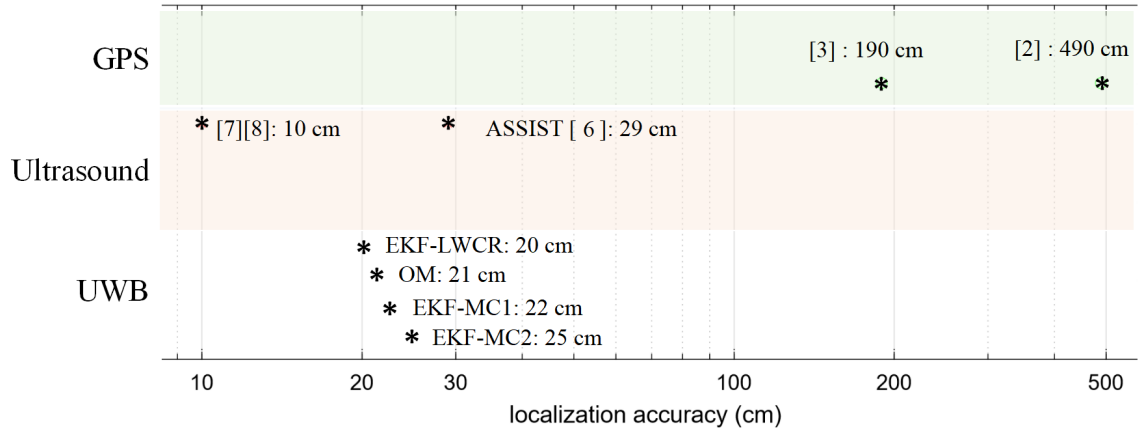
Figure 7.1: Accuracy comparison.

7.2 Future Work

For future endeavors, there is still space for performance enhancement of this localization system. One could try to continue to optimize the setting for the ranging system or change the communication protocol to gain higher sampling rate, measurement obtained rate, and longer measurement range. One could introduce the LWCR to the OM to make the OM more robust in the presence of NLOS errors. One could also try to use LWCR to identify and remove the NLOS measurements, then use only the LOS measurements for estimation.

Bibliography

[1] Bertrand T Fang. Trilateration and extension to global positioning system navigation. *Journal of Guidance, Control, and Dynamics*, 9(6):715–717, 1986.

[2] F van Diggelen and P Enge. The world's first GPS MOOC and worldwide laboratory using smartphones. In *Proceedings of the 28th International Technical Meeting of The Satellite Division of the Institute of Navigation (ION GNSS+ 2015)*, pages 361–369, 2015.

[3] J William. Global positioning system (GPS) standard positioning service (SPS) performance analysis report. *Federal Aviation Administration, Washington, DC Google Scholar*, 2007.

[4] W. Mir and W. Masood. GPS Technology. In *Students Conference, 2002. ISCON '02. Proceedings. IEEE*, volume 2, pages 27–39, Aug 2002. doi: 10. 1109/ISCON.2002.1214579.

[5] Mike Hazas and Andy Hopper. Broadband ultrasonic location systems for improved indoor positioning. *IEEE Transactions on mobile Computing*, 5(5): 536–547, 2006.

[6] Fabian Höflinger, Rui Zhang, Joachim Hoppe, Amir Bannoura, Leonhard M Reindl, Johannes Wendeberg, Manuel Bührer, and Christian Schindelhauer. Acoustic self-calibrating system for indoor smartphone tracking (assist). In *Indoor Positioning and Indoor Navigation (IPIN), 2012 International Conference on*, pages 1–9. IEEE, 2012.

[7] Carlos Medina, José C Segura, and Sverre Holm. Feasibility of ultrasound positioning based on signal strength. In *Indoor Positioning and Indoor Navigation (IPIN), 2012 International Conference on*, pages 1–9. IEEE, 2012.

[8] precise self-calibration of ultrasound based indoor localization systems.

[9] Faheem Zafari, Athanasios Gkelias, and Kin Leung. A Survey of Indoor Localization Systems and Technologies. *arXiv preprint arXiv:1709.01015*, 2017.

[10] Jeffrey Reed. *Introduction to ultra wideband communication systems, an.* Prentice Hall Press, 2005.

[11] Cam Nguyen and Meng Miao. Fundamentals of UWB Impulse Systems. In *Design of CMOS RFIC Ultra-Wideband Impulse Transmitters and Receivers*, pages 7–24. Springer, 2017.

[12] Fehrenbach Patrick. Energieeffiziente Lokalisierungssysteme für die Positions-bestimmung von Objekten im Innenraum auf der Basis von Ultra-wideband, Master thesis, IMTEK, Uni-Freiburg.

[13] Isaac Amundson and Xenofon Koutsoukos. A survey on localization for mobile wireless sensor networks. *Mobile entity localization and tracking in GPS-less environnments*, pages 235–254, 2009.

[14] Yiu-Tong Chan, Wing-Yue Tsui, Hing-Cheung So, and Pak-chung Ching. Time-of-arrival based localization under NLOS conditions. *IEEE Transactions on Vehicular Technology*, 55(1):17–24, 2006.

[15] Pi-Chun Chen. A non-line-of-sight error mitigation algorithm in location estimation. In *Wireless Communications and Networking Conference, 1999. WCNC. 1999 IEEE*, volume 1, pages 316–320. IEEE, 1999.

[16] K. Fukuda and E. Okamoto. Performance improvement of TOA localization using IMR-based NLOS detection in sensor networks. In *The International Conference on Information Network 2012*, pages 13–18, Feb 2012. doi: 10.1109/ICOIN.2012.6164341.

[17] Jeff Foerster, Evan Green, Srinivasa Somayazulu, David Leeper, et al. Ultra-wideband technology for short-or medium-range wireless communications. In *Intel technology journal*. Citeseer, 2001.

[18] Liisa Parv. The Story Behind UWB Technology and Indoor Positioning. `https://www.eliko.ee/uwb-technology-indoor-positioning/`. Accessed January 10, 2018.

[19] Rakhesh Singh Kshetrimayum. An introduction to UWB communication systems. *IEEE Potentials*, 28(2):9–13, 2009.

[20] DW1000 USER MANUAL. Version 2.05, 2015.

[21] Fabian Höflinger. *Lokalisierungssysteme für die Positionsbestimmung von Personen und Objekten im Innenraum*. Der Andere Verlag, 2014.

[22] Gary Bishop, Greg Welch, et al. An introduction to the Kalman filter. *Proc of SIGGRAPH, Course*, 8(27599-23175):41, 2001.

[23] Konrad Reif, Stefan Gunther, Engin Yaz, and Rolf Unbehauen. Stochastic stability of the discrete-time extended Kalman filter. *IEEE Transactions on Automatic control*, 44(4):714–728, 1999.

[24] Introduction to HTerm. `http://www.der-hammer.info/terminal/`. Accessed December 11, 2017.

[25] Hubert Lilliefors. On the Kolmogorov Smirnov test for normality with mean and variance unknown. *Journal of the American Statistical Association*, 262 (5242):399–402, 1967.

[26] Hervé Abdi and Paul Molin. Lilliefors/Van Soest's test of normality. *Encyclopedia of measurement and statistics*, pages 540–544, 2007.

[27] R. A. El-Khoribi, H. S. Hamza, and M. A. Hammad. Indoor localization and tracking using posterior state distribution of hidden markov model. pages 557–562, Aug 2013. doi: 10.1109/ChinaCom.2013.6694657.

[28] Johannes Wendeberg, Fabian Höflinger, Christian Schindelhauer, and Leonhard Reindl. Calibration-free TDOA self-localisation. *Journal of Location Based Services*, 7(2):121–144, 2013. doi: 10.1080/17489725.2013.796410. URL `https://doi.org/10.1080/17489725.2013.796410`.

[29] Serge Gratton, Amos S Lawless, and Nancy K Nichols. Approximate gauss–newton methods for nonlinear least squares problems. *SIAM Journal on Optimization*, 18(1):106–132, 2007.

[30] Henri Gavin. The Levenberg-Marquardt method for nonlinear least squares curve-fitting problems. 2011. *Availble Online from: http://people. duke. edu/˜ hpgavin/ce281/lm. pdf..(Accessed 15 Sept 2015)*, 2016.

[31] Nick Carey. Establishing pedestrian walking speeds. *Karen Aspelin, Portland State University*, 1(01), 2005.

[32] Samuel Sanford Shapiro and Martin B Wilk. An analysis of variance test for normality (complete samples). *Biometrika*, 52(3/4):591–611, 1965.

Acknowledgment

This thesis would have not been possible without the help and support of the amicable people around. My sincere gratitude goes first and foremost to my advisors Fabian Höflinger and Rui Zhang for their constant guidance, enormous efforts and time invested in my thesis. As this thesis is both challenging and entails a large workload, problems emerge from time to time. But for their proficient skills, unrelenting efforts and meticulous working attitude, the problem would not be solved. I learned a lot from them both in the aspect of expanding knowledge in relevant areas and being more professional in scientific research.

Besides, I am greatly thankful to Prof. Dr. Leonhard Reindl and PD Dr. Rüdiger Quay for providing me suggestions and constructive ideas for the perfection of my thesis.

Moreover, I appreciate Johannes Wendeberg for his suggestion to use optimization method, Rui Zhang and Joan Bordoy for helping me collecting measurements data.

In addition, I would extend my appreciation to all the friendly people in Telocate, Fabian Höflinger, Rui Zhang, Johannes Wendeberg, Joachim Hoppe, Joan Bordoy, Sebastian Sester, Simon Päusch and Dominik Jan Schott. They have offered me great supports when I have problems regarding hardware and software during my thesis.

Last but not least, I would like to thank my family for their financial and spiritual supports, and also thank my friends for their accompany during my study in Freiburg.